

UNIVERSITÀ CATTOLICA DEL SACRO CUORE  
SEDE DI BRESCIA

Facoltà di Scienze Matematiche, Fisiche e Naturali  
Corso di Laurea Magistrale in Fisica



Tesi di Laurea

Generation and Detection of  
Terahertz pulses for time-domain  
spectroscopy

*Relatore:*

Dott. Claudio Giannetti

*Correlatori:*

Dott. Francesco Banfi

Dott. Gabriele Ferrini

*Candidato:*

Elia Rampi

*Matricola n.* 3910120

Anno Accademico 2011-2012

# Contents

<b>Introduction</b>	<b>1</b>
<b>1 Generation and Detection of THz pulses</b>	<b>5</b>
1.1 THz Generation . . . . .	5
1.1.1 Nonlinear Effect: Optical Rectification . . . . .	6
1.1.2 Noncentrosymmetric Media . . . . .	8
1.1.3 Rectified Polarization Induced by an Optical Pulse . . . . .	10
1.1.4 Terahertz Pulse Propagation through the Crystal . . . . .	13
1.1.5 The Velocity Matching . . . . .	17
1.1.6 Absorption of ZnTe crystal at Thz frequency . . . . .	19
1.1.7 Crystal Angles and Beams Polarizations . . . . .	20
1.2 THz Detection . . . . .	25
1.2.1 Electro-optical Sampling . . . . .	25
<b>2 Experimental Setup</b>	<b>31</b>
2.1 Laser System . . . . .	32
2.2 Parabolic Mirrors . . . . .	37
2.3 $\lambda/2$ Plate and Polarizer . . . . .	37
2.4 THz Box . . . . .	39
2.5 Lock-in Amplifier . . . . .	39
2.6 Acquisition System . . . . .	41
<b>3 Experimental Results</b>	<b>43</b>
3.1 Signal Acquisition and Optimization . . . . .	43
3.2 In Air Measurements . . . . .	47
3.3 In Nitrogen Measurements . . . . .	48
3.4 The Axes Problem . . . . .	49

---

3.5	High Phase Sensitivity . . . . .	50
<b>4</b>	<b>Determination of Optical Properties</b>	<b>54</b>
4.1	Paper Refractive Index . . . . .	56
<b>5</b>	<b>THz Time-Domain Spectroscopy Measurements</b>	<b>59</b>
5.1	CuGeO <sub>3</sub> . . . . .	59
5.2	Organic-Inorganic Hybrid . . . . .	61
5.3	Biological Samples . . . . .	63
	<b>Conclusions</b>	<b>66</b>
	<b>Bibliography</b>	<b>68</b>

# Introduction

Terahertz (THz) radiation is the electromagnetic radiation whose frequency lies between the microwave and infrared spectrum regions. The THz spectral

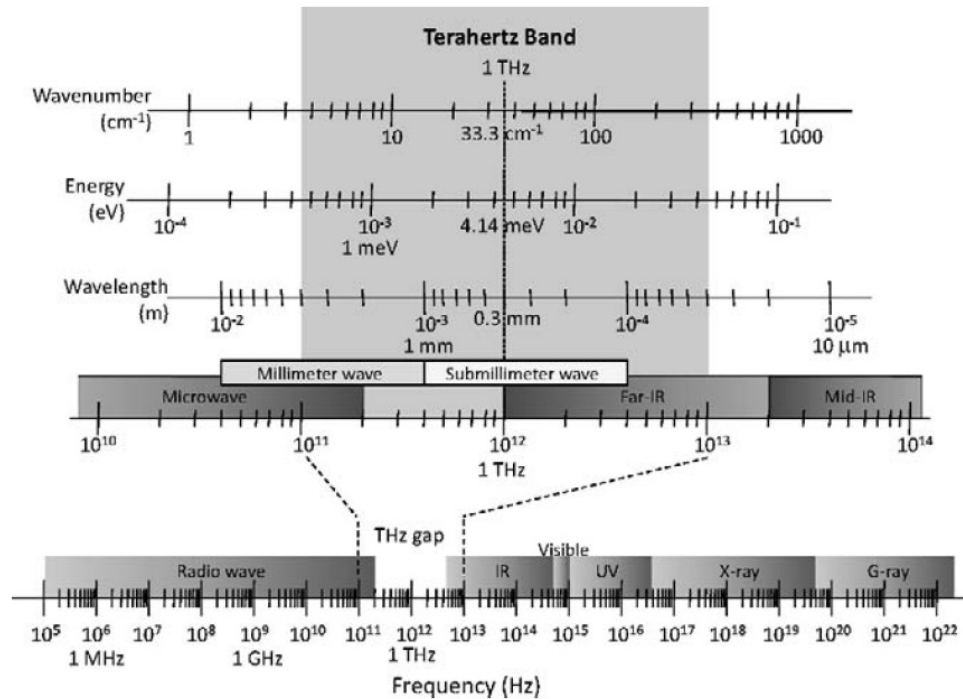


Figure 1: Overview of frequency regions.

band takes its name from the radiation frequency unit and includes the spectral region between 0.1 and 10 THz. Figure 1 illustrates the THz band in the electromagnetic spectrum. This band connects and merges into neighbouring spectral bands which are the microwave and infrared bands.

Frequently used units and their conversions at 1 THz are as follows:

- Frequency:  $\nu = 1 \text{ THz}$

- 
- Angular frequency:  $\omega = 2\pi\nu = 6.28$  THz
  - Period:  $\tau = 1/\nu = 1$  ps
  - Wavelength:  $\lambda = c/\nu = 0.3$  mm =  $300$   $\mu\text{m}$
  - Wavenumber:  $\bar{k} = k/2\pi = 1/\lambda = 33.3$   $\text{cm}^{-1}$
  - Photon energy:  $h\nu = \hbar\omega = 4.14$  meV
  - Temperature:  $T = h\nu/k_B = 48$  K

where  $c$  is the speed of light in vacuum,  $h$  the Plank constant and  $k_B$  the Boltzmann constant.

Although the THz radiation fills up the space of our everyday life, this part of electromagnetic spectrum is the least explored region because of technical difficulties relating sources and detectors.

Because of the absence of suitable technologies, the THz band was called the "THz gap". In fact this gap arises from the nature of the sources and detectors used in spectroscopy both at the optical (high-frequency) side and electronic (low-frequency) side of the gap. This technological gap is rapidly diminished from the early 1980's with the first experiments on generation of picosecond pulses on semiconductor structures [1][2]. Terahertz-Time-Domain-Spectroscopy becomes a valuable tool to study the radiation-matter interaction in terahertz frequency range.

One terahertz corresponds to a photon energy of about 4 meV. This energy is much less than the electronic transitions of atoms and molecules but corresponds to the resonance energy of rotational frequencies of small molecules and vibrational modes of large molecules. Vibrational motion in biological molecules is often characterized by a relaxation dynamics on the picosecond timescale, and can therefore be studied by THz spectroscopy [5] [6]. The vibrational modes involve the intramolecular dynamics of stretch, bend, and torsion among bonded atoms.

Terahertz frequency radiation can penetrate fabrics and plastics and possesses a unique combination of properties for noninvasive imaging and spectroscopy of materials of security interest such as explosives and drugs which have a characteristic spectrum in THz range [7].

Some speculate that there is a big opportunity for THz imaging technologies to make a huge impact in medical applications [8]. A big advantage of THz applications in medicine is that a THz imaging device utilizes a noninvasive, nonionizing, and noncontact probe. A medical imaging device based on THz radiation is, therefore, inherently gentle to the human body. So far, THz imaging has been applied to spotting the onset of cancer, characterizing burn injuries, detecting tooth decay, etc.

A considerable advantage of THz spectroscopy is that the amplitude and phase of the electric field can be measured directly, because the THz fields are coherent with the femtosecond pulses from which they are generated. Using THz time domain spectroscopy, both the real and imaginary parts of the response functions, such as the dielectric function, refractive index, absorption coefficient and optical conductivity are obtained directly without the need of Kramers-Kronig transforms.

THz spectroscopy is useful also for optical pump - THz probe experiments for investigation of non-stationary processes in condensed matter on the picosecond or subpicosecond time scale. This technique is used to study the changes of material permittivity upon photoexcitation with an optical pump pulse. Changes in the permittivity arise from phenomena such as the photoinduced creation of mobile electrons and holes, polarizable excitons, and polarons. These induced changes of sample properties are then probed by a THz pulse.

The interaction of THz radiation with condensed matter is also an interesting subject. Terahertz regime is particularly rich of many important resonances. This includes ubiquitous lattice vibrations and low-energy collective oscillations of conduction charges. In nanoscale materials, band structure quantization also yields novel IR and THz transitions, including intersubband absorption in quantum wells. The formation of excitons in turn leads to low-energy excitations analogous to interlevel transitions in atoms. In transition-metal oxides, fundamental excitation gaps arise from charge pairing into superconducting condensates and other correlated states. This motivates the use of ultrafast THz spectroscopy as a powerful tool to study light-matter interactions and microscopic processes in nanoscale and correlated-electron materials.

Semiconductors provide equally interesting and fundamental excitations

at energies far below their valence-to-conduction band gaps which are typically of 1-2 eV. Here, time domain THz and optical pump THz probe studies are powerful techniques to discern excitations that remain inaccessible to visible light and to probe conduction processes at frequencies comparable to relaxation processes in these materials.

THz time domain spectroscopy is a useful experimental tool to study superconductors [3] [4] [9]. The advantage of THz probes is that they significantly penetrate inside the bulk of the material to provide a contactless probe of low-energy excitations such as the superconducting energy gap and the collective superfluid condensate and quasiparticle response.

THz spectroscopy with optical photoexcitation, is probably the most insightful experimental approach to interrogate non-equilibrium dynamics in superconductors. Such experiments have the potential to measure quasiparticle interactions that remain hidden in linear spectroscopic measurements.

The aim of this work is the realization of a terahertz setup for time domain spectroscopy. It consists in three main sections.

In chapter 2 we will discuss the nonlinear optical methods to generate and detect THz pulses with ZnTe crystals: optical rectification for generation process and electro-optic effect for the detection process. We also explain some other effects concerning the light-matter interaction in these two processes such as the THz pulse propagation through a nonlinear and dispersive crystal, the velocity matching, absorptions and a description of the THz pulse behaviour at different crystal angles and beams polarizations.

In chapters 3 and 4 the experimental setup and the acquisition processes of static time domain THz spectroscopy are described.

In chapter 5 and 6 we describe the unique capability of THz spectroscopy measuring the optical properties of condensed matter systems. Then we conclude with measurements on a  $\text{CuGeO}_3$  crystal, on a organic-inorganic hybrid and on two biological samples, sucrose and blood.

# Chapter 1

## Generation and Detection of THz pulses

There are two main methods to produce and detect THz pulses: an optical method, based on nonlinear effects of some crystals, and a photoconductive method which employs photoconductive antennas. In this work we will use an optical method for generation as well as detection. A wide range of materials has been investigated in literature for these aims and we will use the most efficient one: zinc telluride (ZnTe), which has excellent properties for THz generation and detection.

In this chapter we will to explain the optical phenomena responsible of the generation and detection of THz pulses.

### 1.1 THz Generation

In this section we focus our attention on optical phenomena in nonlinear crystals in order to understand the THz generation schemes exploiting optical rectification, a second-order nonlinear optical effect. The response of the electrons in materials to external electromagnetic waves is the primary source of most optical phenomena. Electromagnetic waves force electrons to move, and the motion of the electrons accelerated in the electric field produces radiation. Usually, the amplitude of the motion of the electrons is very small, and the influence of magnetic fields is almost negligible. Consequently, the optical response of a medium is dominated by the electric dipole oscillations

of the electrons.

In the linear optical regime, the electric dipole moments are proportional to the amplitude of the applied optical field. We assume that electrons bound into the atoms oscillate around their equilibrium positions with a very small amplitude, so that each bound electron behaves as a simple harmonic oscillator. Figure 1.1 illustrates the harmonic oscillator model.

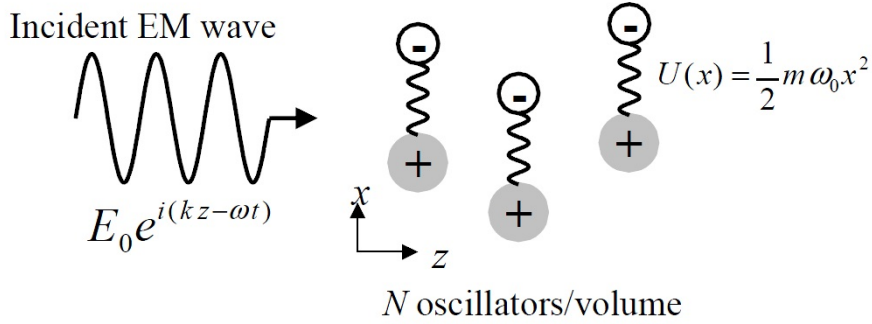


**Figure 1.1:** *The harmonic oscillator model accounts for the linear optical response of bound electrons in a dielectric medium.*

Lorentz model, shows that the bulk polarization for  $N$  electrons per unit volume is proportional to the applied electric field:

$$P(t) = Nex(t) = \frac{Ne^2}{m} \frac{E_0 e^{-i\omega t}}{\omega_0^2 - \omega^2 - i\omega\gamma} = \epsilon_0 \chi(\omega) E_0 e^{-i\omega t} \propto E(t) \quad (1.1)$$

In this linear regime the optical response of the medium oscillates at the same frequency as the external field.

If the applied optical field is considerably strong, nonlinear optical phenomena are generated. In this case, the optical properties of the illuminated material change because of the nonlinear motion of electrons with relatively large amplitude.

### 1.1.1 Nonlinear Effect: Optical Rectification

In the case of linear optics, the induced polarization linearly depends on the electric field

$$P(t) = \epsilon_0 \chi^{(1)} E(t). \quad (1.2)$$

where  $\chi^{(1)}$  is known as the linear susceptibility. In nonlinear optics, the optical response can be described by generalizing Eq. 1.2 and expressing the polarization  $P(t)$  as a power series in the field  $E(t)$ :

$$\begin{aligned} P(t) &= \epsilon_0 \chi^{(1)} E(t) + \epsilon_0 \chi^{(2)} E(t)^2 + \epsilon_0 \chi^{(3)} E(t)^3 + \dots \\ &= P^{(1)} + P^{(2)} + P^{(3)} + \dots \end{aligned} \quad (1.3)$$

The quantities  $\chi^{(2)}$  and  $\chi^{(3)}$  are known respectively as the second- and third-order nonlinear optical susceptibilities. We point out that, for simplicity, we have considered the fields  $P(t)$  and  $E(t)$  as scalar quantities; in the vector description of these fields,  $\chi^{(1)}$  becomes a second-rank tensor,  $\chi^{(2)}$  becomes a third-rank tensor, etc.

Let us consider a particular nonlinear optical interaction, the second-harmonic generation. A laser beam whose electric field is represented as

$$E(t) = E e^{-i\omega t} + c.c. \quad (1.4)$$

is incident upon a crystal for which the second-order susceptibility  $\chi^{(2)}$  is nonzero. The nonlinear polarization that is created in such a crystal is given, according to Eq. 1.3, as  $P^{(2)}(t) = \chi^{(2)} E^2(t)$ , so,

$$P^{(2)}(t) = 2\chi^{(2)} E E^* + (\chi^{(2)} E^2 e^{-i2\omega t} + c.c.). \quad (1.5)$$

We see that the second-order polarization consists in a contribution at nonzero frequency (first term) and a contribution at  $2\omega$  frequency (second term). According to the wave equation in nonlinear optical media [10]

$$\nabla^2 E - \frac{n^2}{c^2} \frac{\partial^2 E}{\partial t^2} = \frac{4\pi}{c^2} \frac{\partial^2 P^{NL}}{\partial t^2}, \quad (1.6)$$

the latter contribution can lead to the radiation generation at the second-harmonic frequency. The first contribution in Eq. 1.5 does not lead to the generation of electromagnetic radiation because its second time derivative vanishes; it leads to a process known as optical rectification in which a static electric field is created within the nonlinear crystal. This effect is of our interest because optical rectification is one of the main mechanisms for the generation of terahertz radiation.

### 1.1.2 Noncentrosymmetric Media

In order to describe the THz generation, we study nonlinear interactions with noncentrosymmetric media, and in particular the case of ZnTe crystal. Figure 1.2 shows its crystal structure.

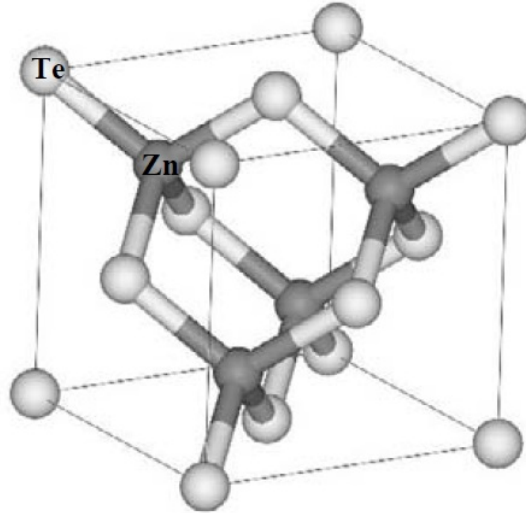


**Figure 1.2:** *ZnTe crystal structure.*

ZnTe is noncentrosymmetric. This means that it has no inversion symmetry. Te has a electronegativity larger than Zn, so the distribution of electron charge in a chemical bond inclines toward Te. The asymmetric charge distribution gives rise to an asymmetric potential energy along the chemical bond. An approximation of the potential energy function is a Taylor series expansion about the equilibrium position. Figure 1.3 shows a model potential energy in which the cubic term of the Taylor series is included to represent the asymmetry of the chemical bond. When the electron motion is sufficiently large, the discrepancy between the positive and negative displacements becomes important. Figure 1.3(b) illustrates the nonlinear electron motion, which is decomposed into linear ( $x_L(t)$ , dashed line) and nonlinear ( $x_{NL}(t)$ , dashed-dotted line) parts. The nonlinear part consists of two frequency components (Fig. 1.3(c)) representing the two prominent nonlinear optical processes: second harmonic generation (SHG) and optical rectification.

The equation of motion for the Lorentz model revised to incorporate the

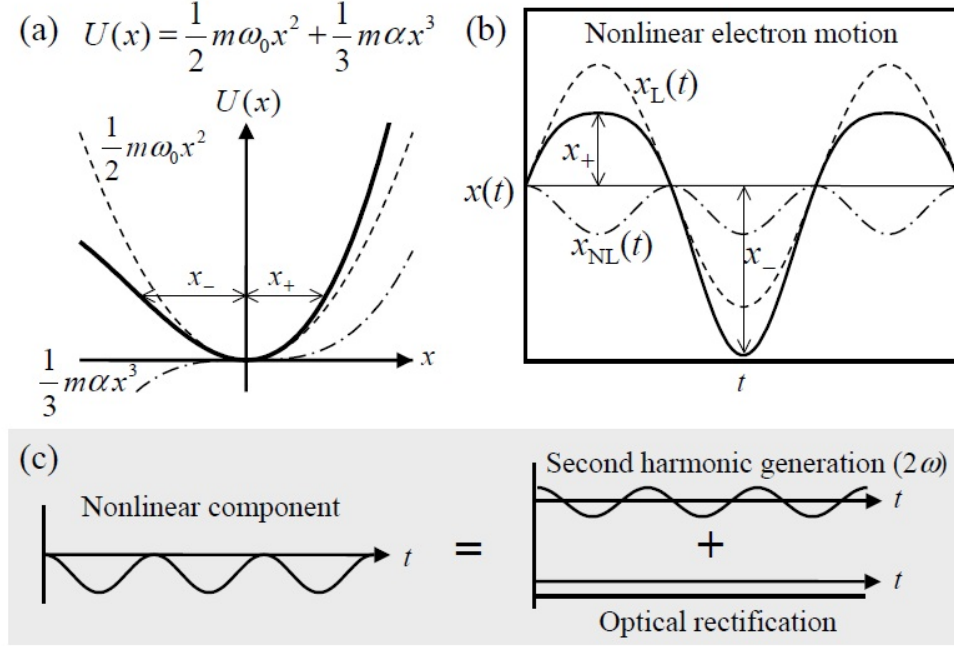


**Figure 1.3:** Electric potential energy and nonlinear motion for an electron in a noncentrosymmetric medium.

nonlinear responses has the form

$$\frac{d^2x}{dt^2} + \gamma \frac{dx}{dt} + \omega_0^2 x + \alpha x^2 = -\frac{e}{m} E(t). \quad (1.7)$$

We assume that the incident wave is monochromatic:

$$E(t) = E_0 e^{-i\omega t}. \quad (1.8)$$

In the perturbative regime where the nonlinear term  $\alpha x^2$  is much smaller than the linear term  $\omega_0^2 x$ , it is valid to expand  $x(t)$  as

$$x(t) = \sum_{n=1}^{\infty} x^{(n)}(t), \quad n = 1, 2, 3, \dots \quad (1.9)$$

where  $x^{(n)} \propto (E_0)^n$ . We can apply a perturbation procedure to obtain the  $n$ -th order solution  $x^{(n)}$ , assuming that the solution is convergent, i.e.,  $x^{(1)} \gg x^{(2)} \gg x^{(3)} \dots$ , in the limit of a relatively small nonlinearity. By substituting Eq. 1.9 into Eq. 1.7 and equating terms of equivalent frequency dependence,

we obtain the equations for the first and second-order terms,

$$\frac{d^2x^{(1)}}{dt^2} + \gamma \frac{dx^{(1)}}{dt} + \omega_0^2 x^{(1)} = -\frac{e}{m} E(t), \quad (1.10)$$

$$\frac{d^2x^{(2)}}{dt^2} + \gamma \frac{dx^{(2)}}{dt} + \omega_0^2 x^{(2)} = -\alpha [x^{(1)}]^2. \quad (1.11)$$

The first-order (linear) response at  $\omega$  is

$$x^{(1)}(t) = -\frac{e}{m} \frac{E_0 e^{-i\omega t}}{\omega_0^2 - \omega^2 - i\omega\gamma} + c.c., \quad (1.12)$$

and substituting Eq. 1.12 into Eq. 1.11, we obtain the second-order responses corresponding to SHG at  $2\omega$  and optical rectification:

$$\begin{aligned} x^{(2)}(t) = & -\alpha \left[ \frac{eE_0}{m} \right]^2 \frac{e^{-i2\omega t}}{(\omega_0^2 - \omega^2 - i\omega\gamma)^2 (\omega_0^2 - (2\omega)^2 - i2\omega\gamma)} + c.c. \\ & - 2\alpha \left[ \frac{e}{m\omega_0} \right]^2 \frac{|E_0|^2}{(\omega_0^2 - \omega^2)^2 + \omega^2\gamma^2}. \end{aligned} \quad (1.13)$$

The bulk polarization induced by optical rectification is [10]:

$$\begin{aligned} P_0^{(2)} = & -Nex_0^{(2)} = \frac{2\alpha e^2 N}{m^2 \omega_0^2 ((\omega_0^2 - \omega^2)^2 + \omega^2 \gamma^2)} |E_0|^2 \\ = & 2\epsilon_0 \chi^{(2)}(0, \omega, -\omega) |E_0|^2, \end{aligned} \quad (1.14)$$

where  $\chi^{(2)}(0, \omega, -\omega)$  is the second-order nonlinear optical susceptibility corresponding to the optical rectification process. We must point out that the static nonlinear polarization is proportional to the applied light intensity.

### 1.1.3 Rectified Polarization Induced by an Optical Pulse

Now we consider a rectified polarization induced by an optical pulse instead of a continuous wave. An optical pulse is expressed as  $E(t) = E_0(t)e^{-i\omega t}$  with the time-dependent field amplitude  $E_0(t)$ . Assuming the pulse duration  $\tau_p$  is much longer than the optical period  $\tau_p \gg \omega^{-1}$  and the dispersion of the nonlinear susceptibility is negligible near the optical frequency, the rectified nonlinear polarization replicates the optical pulse envelope. Figure 1.4 shows the electric field of a Gaussian optical pulse and corresponding nonlinear

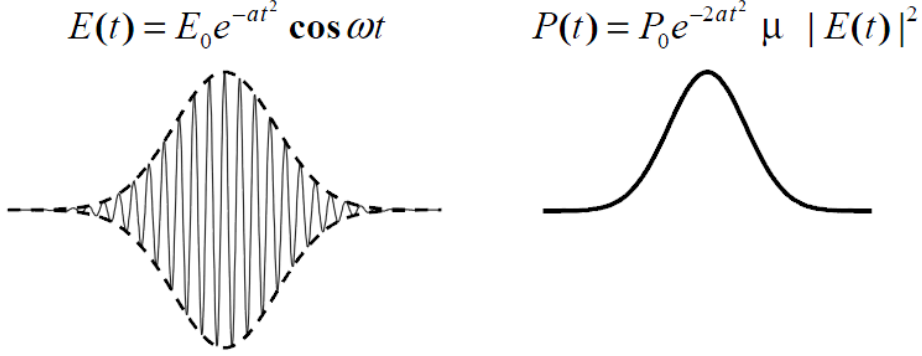


**Figure 1.4:** Applied optical field of a Gaussian pulse and nonlinear polarization induced by optical rectification.

polarization induced by optical rectification. As in linear case, the time varying polarization is a source of electromagnetic radiation. If we consider the case of a point source, i.e. of size much smaller than the generated wavelength, the emitted electric field is proportional to the second derivative of the induced polarization:

$$E_{THz}(t) \propto \frac{\partial^2 P(t)}{\partial t^2}. \quad (1.15)$$

In figure 1.5 are shown the optical pulse, the induced polarization and the respective THz field ideally produced by a infinitesimally thin crystal located in  $z'$ .

To better explain how the THz beam is produced, let us see the pulses in frequency domain. We consider a gaussian optical pulse

$$E(t) = E_0 e^{-a_0 t^2} e^{-i\omega_0 t}, \quad (1.16)$$

with  $FWHM = \sqrt{\frac{2 \ln 2}{a_0}}$ , and its Fourier transform

$$E(\omega) = \sqrt{\frac{\pi}{a_0}} E_0 e^{-(\omega - \omega_0)^2 / 4a_0} \quad (1.17)$$

As we can see from equation 1.17 and in Figure 1.6 the optical pulse transform is a gaussian wave centred on the beam frequency  $\omega_0$ . Optical rectification can also be understood as the difference frequency generation

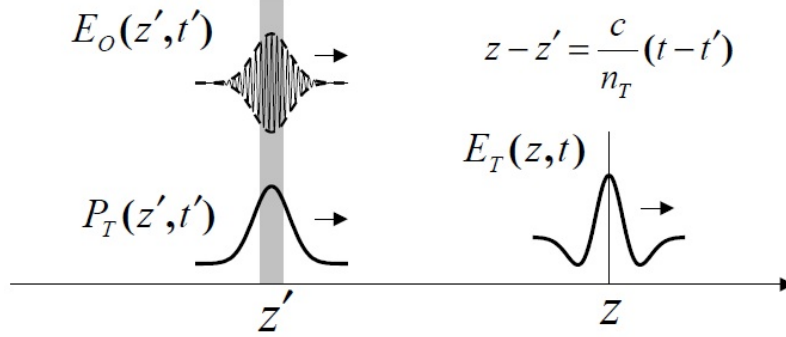


**Figure 1.5:** THz dipole radiation from a thin layer of nonlinear polarization generated by a Gaussian optical pulse.

between these frequencies; we observe that the frequency width of this wave sets the maximum frequency of the beam produced. In the frequency domain nonlinear polarization is

$$P^{(2)}(\omega_1 - \omega_2) = \epsilon_0 \chi^{(2)} E(\omega_1) E(\omega_2), \quad (1.18)$$

where  $\omega_1$  and  $\omega_2$  can be any two frequencies of the pulse spectrum. Thus, the THz spectrum is composed of frequencies from zero to maximal frequency, determined by the width of the gaussian wave. As we can see in Figure 1.7 the largest contribution comes from the frequencies close to the maximum (red lines), whose difference gives to the spectrum a contribution at very low frequency. The difference of frequencies away from the center of the gaussian (blue lines) gives a smaller contribution due to the gaussian profile of the spectrum.

Optical pulses with different time width generate spectra with different bandwidth; the shorter is the pulse, the larger is the bandwidth.

An important point to understand the generation of pulses in THz range is that the refractive index of the generation crystal at THz frequencies is different from the refractive index in vacuum, i.e.  $n > 1$ . Figure 1.8 shows the index wavelength dependence of ZnTe crystal and we can see that at 800 nm is about  $n_{800} \simeq 3.2$ . This means that the optical pulse slows down in the crystal because the group velocity decreases,

$$v_{gr} = \frac{\partial \omega}{\partial k} = c \left( \frac{\partial n(\omega) \omega}{\partial \omega} \right)^{-1}. \quad (1.19)$$

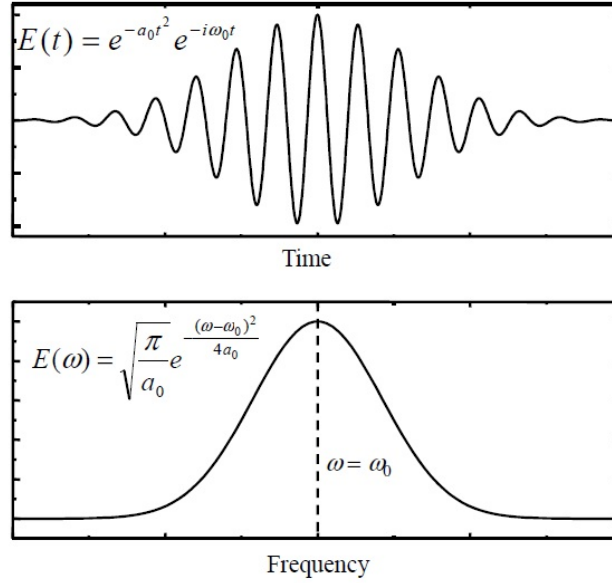


**Figure 1.6:** *Optical pulse in time and frequency domain.*

In our case an optical pulse of about 130 fs is stretched in time to about 400 fs which correspond to a frequency of 2.5 THz, so in frequency range of system resonance. The second order susceptibility  $\chi^{(2)}$  is the parameter which contains the crystal resonance frequencies; the key point is what we use to force the system. In order to have a larger production of THz radiation we must be in resonance with the system creating a nonlinear polarization which its second derivative has a frequency in THz range.

#### 1.1.4 Terahertz Pulse Propagation through the Crystal

In real cases we have to consider not only the THz production by a dipole radiation but also the propagation of this pulse through the crystal which is responsible for a change of the shape of the pulse. To understand this process we describe a gaussian pulse propagation in a dispersive medium. In dispersive media the refractive index depends on the frequency, and the wavenumber can be expressed as

$$k(\omega) = \frac{\omega}{c}n(\omega). \quad (1.20)$$

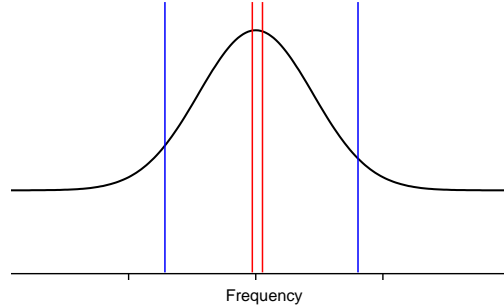


**Figure 1.7:** *Gaussian spectrum of optical pulse.*

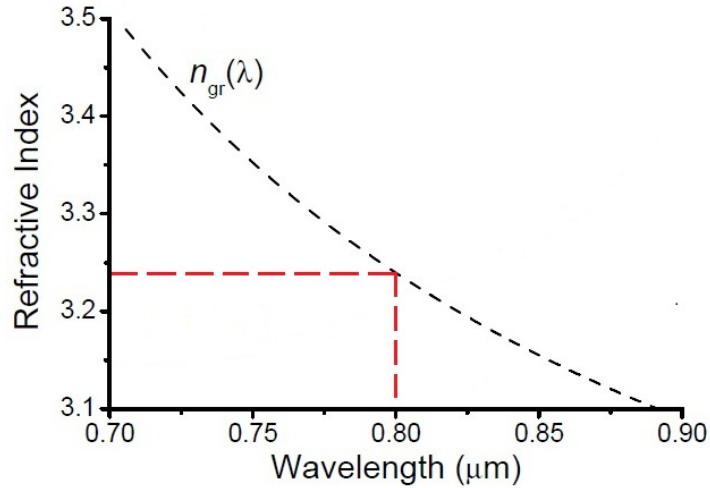


**Figure 1.8:** *Optical group refractive indexes of ZnTe.*

If  $k(\omega)$  varies slowly in the vicinity of the central frequency  $\omega_0$  we can use the second order expansion

$$k(\omega) \simeq k(\omega_0) + k'(\omega_0)(\omega - \omega_0) + \frac{1}{2}k''(\omega_0)(\omega - \omega_0)^2. \quad (1.21)$$

The electric field of equations 1.16 and 1.17, during the propagation along  $z$ , takes a phase factor  $e^{ik(\omega)z}$  and the pulse becomes

$$E(z, \omega) = E(\omega)e^{ik(\omega)z} = E_0 \exp \left\{ ik(\omega_0)z + ik'(\omega_0)z(\omega - \omega_0) + \left[ \frac{ik''(\omega_0)z}{2} - \frac{1}{4a_0} \right] (\omega - \omega_0)^2 \right\} \quad (1.22)$$

and its inverse transform is

$$E(z, t) = E_0 e^{-a(z)\left(t - \frac{z}{v_{gr}}\right)^2} e^{-i\omega_0\left(t - \frac{z}{v_{ph}}\right)} \quad (1.23)$$

where

$$v_{gr} = \left[ \frac{\partial \omega}{\partial k} \right]_{\omega=\omega_0} = \frac{1}{k'(\omega_0)} \quad (1.24)$$

$$v_{ph} = \frac{\omega_0}{k_0} \quad (1.25)$$

are the group and phase velocity respectively, and  $a(z)$  a parameter given by

$$\frac{1}{a(z)} = \frac{1}{a_0} - 2ik''(\omega_0)z. \quad (1.26)$$

Since  $a(z)$  is a complex number, then  $a(z) = a_R(z) + ia_I(z)$  where

$$a_R(z) = \frac{a_0}{1 + 4a_0^2 k''(\omega_0)^2 z^2} \quad (1.27)$$

$$a_I(z) = \frac{2a_0^2 k''(\omega_0)z}{1 + 4a_0^2 k''(\omega_0)^2 z^2}. \quad (1.28)$$

So the first exponential term of equation 1.23 becomes

$$e^{-a_R(z)\left(t - \frac{z}{v_{gr}}\right)^2} e^{-ia_I(z)\left(t - \frac{z}{v_{gr}}\right)^2}. \quad (1.29)$$

From this equation we can see that from the real part  $a_R(z)$  depends the pulse duration since we have

$$FWHM(z) = \sqrt{\frac{2\ln 2}{a_R}} = FWHM(0) \sqrt{1 + 4a_0^2 k''(\omega_0)^2 z^2}, \quad (1.30)$$

i.e. the pulse broadens during the propagation in the dispersive material.

The second part of equation 1.29 means that the imaginary part  $a_I(z)$  introduces in the electric field a quadratic temporal phase term.

The total phase is

$$\phi(t) = \phi_0 + \omega_0 \left( t - \frac{z}{v_{ph}} \right) + a_I \left( t - \frac{z}{v_{gr}} \right)^2, \quad (1.31)$$

than the instant frequency is

$$\omega \equiv \frac{d\phi(t)}{dt} = \omega_0 + 2a_I t', \quad (1.32)$$

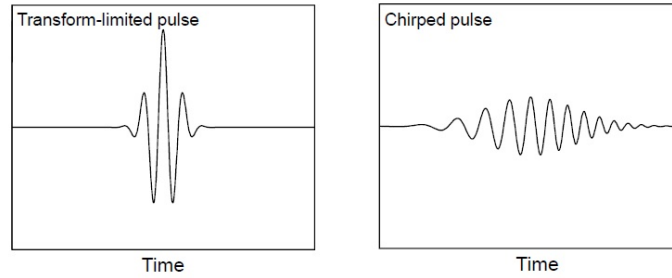


**Figure 1.9:** A gaussian pulse becomes broadened and chirped after propagation in a dispersive medium.

where  $t' = t - \frac{z}{v_{gr}}$  are the pulse coordinates.

We point out that the frequency  $\omega$  varies in time. Such a waveform is called chirped pulse. Figure 1.9 shows the effect of pulse propagation in a dispersive media. The pulse broadens while the field amplitude decreases and the instantaneous frequency increases gradually in the positively-chirped pulse.

This is what happens to the THz pulse propagating through the nonlinear and dispersive crystal as we can see in Figure 1.10.

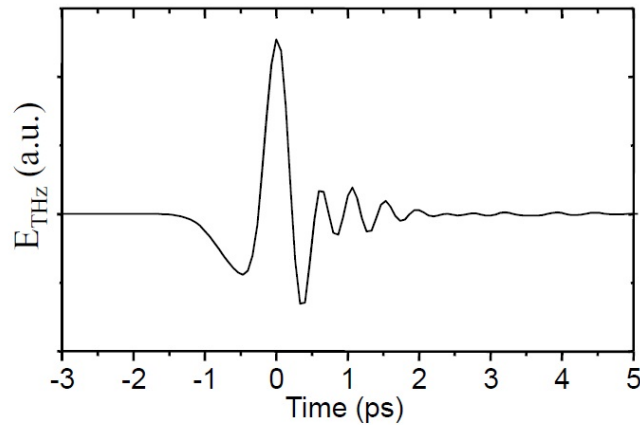


**Figure 1.10:** Temporal waveform of a THz pulse generated by optical rectification in a 1.0-mm thick ZnTe crystal.

### 1.1.5 The Velocity Matching

#### Dispersionless Media

During the THz generation process in the crystal, we have to consider the different propagation velocity of the different frequencies. We first consider a dispersionless medium at THz and optical frequencies, i.e., the refractive indices  $n_T$  and  $n_O$  are independent of frequency. In the ideal case of perfect velocity matching conditions, i.e. in which the THz pulse propagates with the same velocity as the optical pulse ( $n_T = n_O$ ), the THz field is gradually amplified while propagating through the medium as we can see in Figure 1.11, therefore, the THz field is proportional to the propagation length.

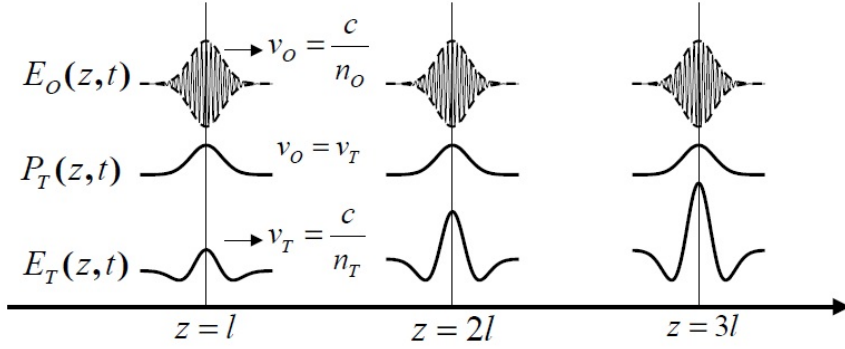


**Figure 1.11:** Linear amplification of THz field in a medium satisfying the velocity matching condition.

In general, the velocity matching condition is difficult to satisfy. When the optical wave is faster than the THz wave ( $n_T > n_O$ ), the optical pulse leads the THz pulse by the optical pulse duration,  $\tau$ , after a walk-off length of

$$l_w = \frac{c\tau_p}{(n_T - n_O)}. \quad (1.33)$$

Imagine two thin layers of nonlinear media separated by the walk-off length, which is illustrated in Figure 1.12. The superposition of the THz radiation fields from the two layers shows destructive interference near  $z = l_w$ . While propagating in a uniform nonlinear medium, the THz radiation field continuously undergoes destructive interference. When the thickness of the

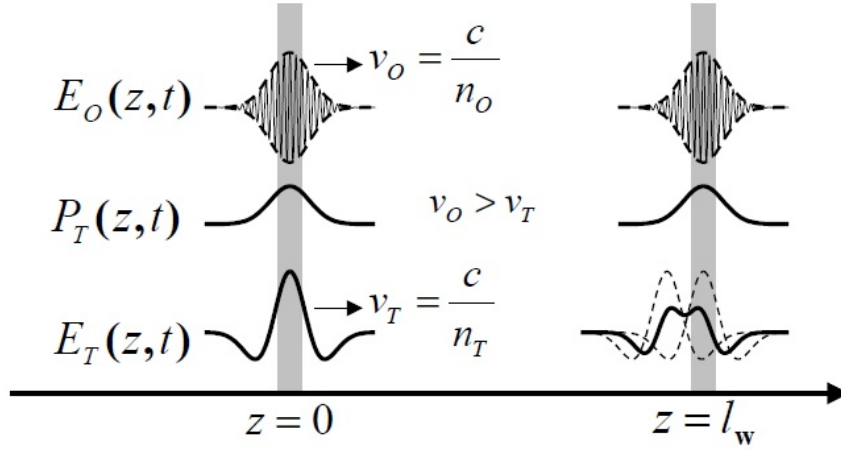


**Figure 1.12:** Destructive interference between the THz radiation fields from two nonlinear layers separated by a walk-off length  $l_w$ . The dotted lines indicate the two THz fields.

nonlinear medium is much longer than the walk-off length ( $l \gg l_w$ ), the total THz field vanishes.

### Dispersive Media

In practice, nonlinear crystals are dispersive media at both optical and THz frequencies: the refractive index  $n_\omega$  varies with frequency. As a result, the group velocity  $v_{gr}$  differs from the phase velocity  $v_{ph}$  at most frequencies. Consequently, velocity matching in a dispersive medium can be achieved only for a certain THz frequency when the optical pulse envelope travels at the phase velocity of the monochromatic THz wave. The optimal velocity matching condition for a broadband THz pulse is that the optical group velocity is the same as the phase velocity of the central frequency of the THz spectrum. ZnTe is the most widely used nonlinear crystal for THz generation because the group refractive index  $n_{gr}(\lambda)$  near the optical wavelength  $\lambda = 800nm$  (the operational wavelength of Ti:sapphire femtosecond lasers) matches well with the THz refractive index  $n_T(\nu_{THz})$ . As we can see in Figure 1.13 the velocity matching condition for ZnTe crystal is satisfied when the optical wavelength is  $\lambda = 812nm$  and the THz frequency

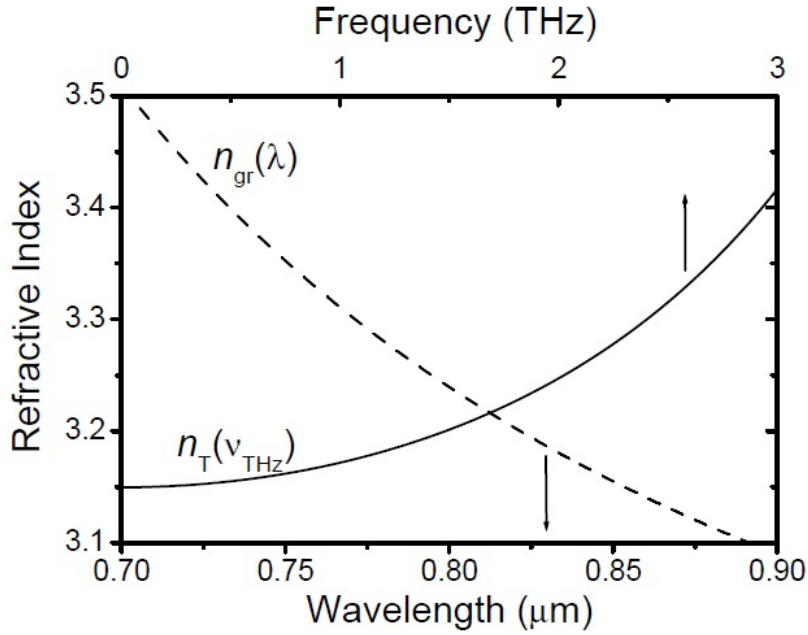


**Figure 1.13:** Optical group refractive indexes  $n_{gr}(\lambda)$  and THz refractive indexes  $n_T(\nu_{THz})$  of ZnTe.

is  $1.69THz$ , therefore,

$$n_{gr}(812\mu m) = n_T(1.69THz) = 3.22. \quad (1.34)$$

### 1.1.6 Absorption of ZnTe crystal at Thz frequency

The spectral bandwidth of THz generation in a nonlinear crystal is limited by absorption in the THz frequency region. The dominant THz absorption processes in EO crystals are the transverse-optical (TO) phonon resonances, which usually lie in the range from 5 to 10 THz. At lower frequencies, second-order phonon processes give rise to weak, yet complicated and broad absorption spectra. Figure 1.14 shows the measured (solid line) absorption coefficient for ZnTe crystal compared to the calculated (dashed line) absorption for the TO-phonon line [11]. ZnTe has a strong TO-phonon resonance at  $\nu = 5.32$  THz at room temperature. The absorption coefficient is expressed as

$$\alpha(\nu) = \frac{4\pi\nu k(\nu)}{c}. \quad (1.35)$$

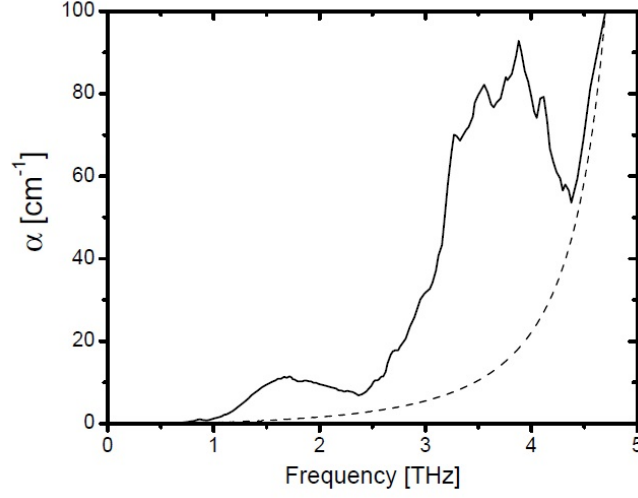


**Figure 1.14:** Absorption coefficient  $\alpha(\nu/\text{THz})$  of ZnTe from 0 to 5THz at room temperature. The dashed line indicates the calculated absorption for the TO-phonon line centred at 5.32 THz.

### 1.1.7 Crystal Angles and Beams Polarizations

It is now necessary to introduce the tensor formalism to properly describe the nonlinear susceptibility of a crystal. We can express the nonlinear polarization induced by optical rectification of Eq. 1.5 as

$$P_i^{(2)}(0) = \sum_{j,k} \epsilon_0 \chi_{ijk}^{(2)}(0, \omega, -\omega) E_j(\omega) E_k^*(\omega). \quad (1.36)$$

The indices  $i$ ,  $j$ , and  $k$  indicate the cartesian components of the fields.  $\chi_{ijk}^{(2)}$  is the second-order nonlinear susceptibility tensor element for the crystal system. When the indices are permutable, we can use the contracted notation [10]:

$$d_{il} = \frac{1}{2} \chi_{ijk}^{(2)}, \quad (1.37)$$

where

$$\begin{array}{l} l = \quad 1 \quad 2 \quad 3 \quad 4 \quad 5 \quad 6 \\ jk = \quad 11 \quad 22 \quad 33 \quad 23, 32 \quad 31, 13 \quad 12, 21 \end{array} \quad (1.38)$$

Using the contracted matrix we can describe the nonlinear polarization as the matrix equation

$$\begin{pmatrix} P_x \\ P_y \\ P_z \end{pmatrix} = 2\epsilon_0 \begin{pmatrix} d_{11} & d_{12} & d_{13} & d_{14} & d_{15} & d_{16} \\ d_{21} & d_{22} & d_{23} & d_{24} & d_{25} & d_{26} \\ d_{31} & d_{32} & d_{33} & d_{34} & d_{35} & d_{36} \end{pmatrix} \begin{pmatrix} E_x^2 \\ E_y^2 \\ E_z^2 \\ 2E_y E_z \\ 2E_z E_x \\ 2E_x E_y \end{pmatrix} \quad (1.39)$$

ZnTe, the most commonly used EO crystal for THz generation and detection, has the crystal class of  $\bar{4}3m$ . This crystal class has three nonvanishing d-matrix elements and only one of them is independent:

$$d_{il} = \begin{pmatrix} 0 & 0 & 0 & d_{14} & 0 & 0 \\ 0 & 0 & 0 & 0 & d_{14} & 0 \\ 0 & 0 & 0 & 0 & 0 & d_{14} \end{pmatrix}. \quad (1.40)$$

When an optical field interacts with ZnTe, the power of the THz radiation produced depends on the direction of the field in the frame of the crystal. An arbitrary field is expressed as

$$\mathbf{E} = E_0 \begin{pmatrix} \sin \theta \cos \phi \\ \sin \theta \sin \phi \\ \cos \theta \end{pmatrix} \quad (1.41)$$

with the polar angle  $\theta$  and the azimuthal angle  $\phi$ . Using Eq. 1.39 we obtain the nonlinear polarization:

$$\begin{aligned} \begin{pmatrix} P_x \\ P_y \\ P_z \end{pmatrix} &= 2\epsilon_0 d_{14} E_0^2 \begin{pmatrix} 0 & 0 & 0 & 1 & 0 & 0 \\ 0 & 0 & 0 & 0 & 1 & 0 \\ 0 & 0 & 0 & 0 & 0 & 1 \end{pmatrix} \begin{pmatrix} \sin^2 \theta \cos^2 \phi \\ \sin^2 \theta \sin^2 \phi \\ \cos^2 \theta \\ 2 \sin \theta \cos \theta \sin \phi \\ 2 \sin \theta \cos \theta \cos \phi \\ 2 \sin^2 \theta \sin \phi \cos \phi \end{pmatrix} \\ &= 4\epsilon_0 d_{14} E_0^2 \sin \theta \begin{pmatrix} \cos \theta \sin \phi \\ \cos \theta \cos \phi \\ \sin \theta \sin \phi \cos \phi \end{pmatrix}. \end{aligned} \quad (1.42)$$

The consequent THz radiation field is parallel to the nonlinear polarization, therefore the intensity of the THz radiation has the angular dependence

$$I_{THz}(\theta, \phi) \propto |\mathbf{P}|^2 = 4\epsilon_0^2 d_{14}^2 \sin^2 \theta (4 \cos^2 \theta + \sin^2 \theta \sin^2 2\phi). \quad (1.43)$$

The THz intensity is maximized when  $\sin^2 2\phi = 1$  ( $\phi = \frac{\pi}{4}$  or  $\frac{3\pi}{4}$ ), i.e., the optical polarization lies in the (110) plane (Figure 1.15). Therefore, the

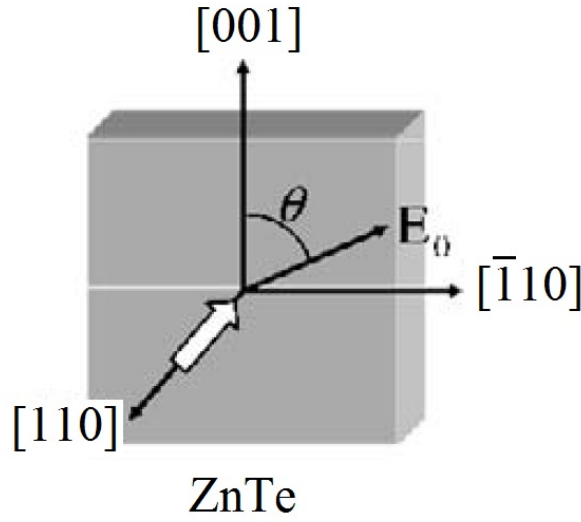


**Figure 1.15:** A linearly polarized optical wave is incident on a (110) ZnTe crystal with normal angle.  $\theta$  is the angle between the optical field and the [001] axis.

radiated THz intensity as a function of  $\theta$  is written as

$$I_{THz}(\theta) = \frac{3}{4} I_{THz}^{max} \sin^2 \theta (4 - 3 \sin^2 \theta). \quad (1.44)$$

The maximum intensity  $I_{THz}^{max}$  is obtained at  $\theta = \sin^{-1} \sqrt{\frac{2}{3}}$ . This angle corresponds to an optical field that is parallel to either the  $[\bar{1}11]$  or  $[1\bar{1}1]$  axis. In other words, we can optimize the THz intensity by aligning the optical field along the chemical bonds between the Zn and the Te (see the crystal structure of ZnTe in Fig. 1.2). Figure 1.16 shows the angle-dependent THz radiation intensity.

We can deduce the expression for the angle-dependent THz field vector

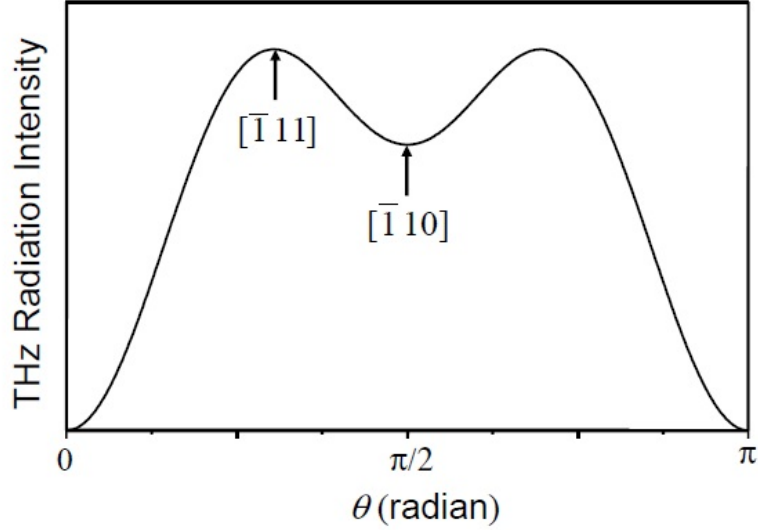


**Figure 1.16:** THz radiation intensity vs  $\theta$  in ZnTe.

from Eq. 1.42:

$$\mathbf{E}_{THz}(\theta) = \frac{\sqrt{3}}{2} E_{THz}^{max} \sin \theta \begin{pmatrix} \sqrt{2} \cos \theta \\ -\sqrt{2} \cos \theta \\ -\sin \theta \end{pmatrix}. \quad (1.45)$$

When the linearly polarized optical field is aligned along the  $[001]$ ,  $[\bar{1}11]$ , or  $[\bar{1}10]$  axis,  $\mathbf{E}_{THz}$  has the relations

$$\begin{aligned} \mathbf{E}_0 // [001] &\rightarrow \mathbf{E}_{THz} = 0, \\ \mathbf{E}_0 // [\bar{1}11] &\rightarrow \mathbf{E}_{THz} = \frac{1}{\sqrt{3}} E_{THz}^{max} \begin{pmatrix} 1 \\ -1 \\ -1 \end{pmatrix} // -\mathbf{E}_0, \\ \mathbf{E}_0 // [\bar{1}10] &\rightarrow \mathbf{E}_{THz} = \frac{\sqrt{3}}{2} E_{THz}^{max} \begin{pmatrix} 0 \\ 0 \\ -1 \end{pmatrix} \perp -\mathbf{E}_0. \end{aligned} \quad (1.46)$$

The THz field is antiparallel to the optical field when the optical field is aligned along the  $[\bar{1}11]$  axes; they are perpendicular to each other when the optical field is parallel to the  $[\bar{1}10]$  axes. The angle  $\alpha$  between the optical and the THz fields as a function of  $\theta$  can be written as

$$\alpha(\theta) = \cos^{-1} \left\{ \frac{\mathbf{E}_0 \cdot \mathbf{E}_{THz}}{|\mathbf{E}_0| |\mathbf{E}_{THz}|} \right\} = \cos^{-1} \left\{ -3 \frac{\sin \theta |\cos \theta|}{\sqrt{4 - 3 \sin^2 \theta}} \right\}, \quad (1.47)$$

which varies between  $90^\circ$  and  $180^\circ$  as is shown in Figure 1.17.

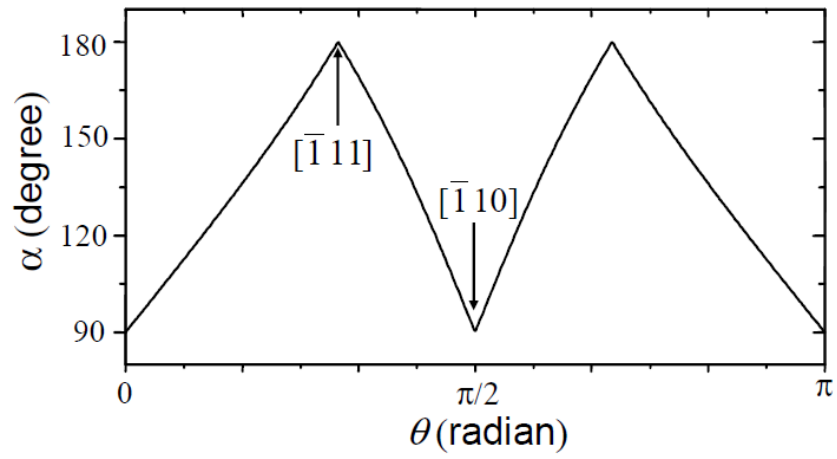


**Figure 1.17:** Angle between the optical and the THz fields as a function of  $\theta$ .

## 1.2 THz Detection

In this section we will explain how the THz pulses can be detected. As in the generation process, we use non linear optical effect of ZnTe crystal known as electro-optic effect or Pockels effect. This effect is closely related to optical rectification, as evident in the similarity between the expressions of second-order nonlinear polarizations. In this case is:

$$\begin{aligned} P_i^{(2)}(\omega) &= 2 \sum_{j,k} \epsilon_0 \chi_{ijk}^{(2)}(\omega, \omega, 0) E_j(\omega) E_k(0) \\ &= \sum_j \epsilon_0 \chi_{ij}^{(2)}(\omega) E_j(\omega), \end{aligned} \quad (1.48)$$

where  $\chi_{ij}^{(2)}(\omega)$  is the field induced susceptibility tensor. In a lossless medium

$$\chi_{ijk}^{(2)}(0, \omega, -\omega) = \chi_{ijk}^{(2)}(\omega, \omega, 0), \quad (1.49)$$

thus the Pockels effect has the same nonlinear optical coefficients as optical rectification. Eq. 1.48 indicates that a static electric field induces birefringence in a nonlinear optical medium proportional to the applied field amplitude. Inversely, the applied field strength can be determined by measuring the field-induced birefringence.

### 1.2.1 Electro-optical Sampling

The electro-optical sampling exploits the Pockels effect to measure the electric field of THz pulses in the time domain, determining not only the amplitude, but also the phase with high precision.

Let us consider two collinear beams that pass through the ZnTe crystal: an optical pulse of 800 nm and the THz pulse. As we can see in Figure 1.18 the optical pulse is spatially much shorter than THz pulse, thus, in the crystal it will experience a constant electric field of the THz pulse while propagating if the optical group velocity matches well with the THz phase velocity in the crystal.

The static electric field responsible for the field-induced birefringence of Pockels effect is the THz pulse. Changing the temporal coincidence of the two pulses, the optical pulse will probe different electric fields which induce different birefringences.

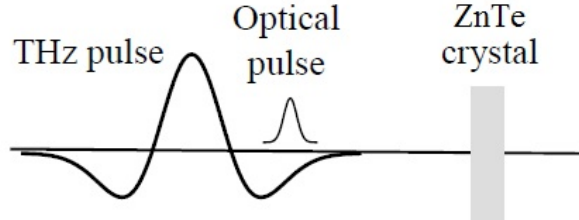


**Figure 1.18:** *The two collinear beams before the ZnTe crystal*

Figure 1.19 illustrates a typical setup of electro optical sampling to measure field-induced birefringence.

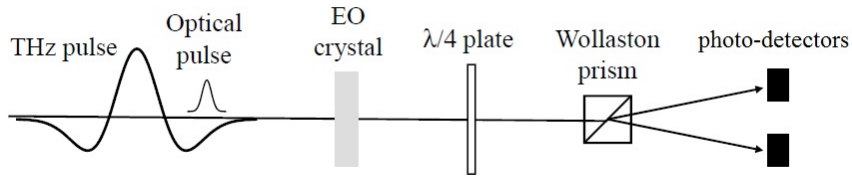


**Figure 1.19:** *Schematic diagram of a typical setup for electro optical sampling.*

Between the crystal and detectors the optical beam passes through two optical elements: a  $\lambda/4$  plate and a Wollaston prism.

### $\lambda/4$ Plate

The  $\lambda/4$  plate is an optical element that introduces a relative phase shift of  $\Delta\phi = \pi/2$  between the orthogonal  $o$ - and  $e$ - components of a wave. This phase shift convert linear to elliptical light and vice versa. It is clear that linear light incident parallel to either principal axis is unaffected by any sort of retardation. When linear light at  $45^\circ$  to either principal axis is incident on the  $\lambda/4$  plate, its  $o$ - and  $e$ - components have equal amplitudes. Under this conditions, a  $90^\circ$  phase shift converts the wave into circular light.

### Wollaston Prism

The Wollaston prism is an optical device that separates randomly polarized or unpolarized light into two orthogonal linearly polarized outgoing beams. This polarizing beam splitter prism consists of two orthogonal calcite prisms, cemented together on their base to form two right triangle prisms with perpendicular optic axes. As we can see in Figure 1.20 the two component

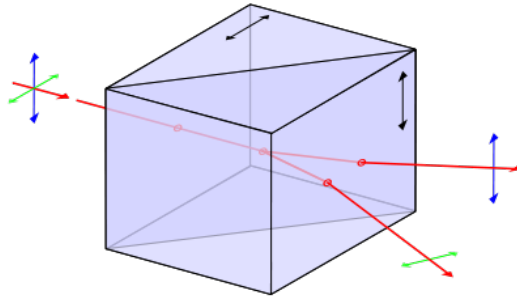


**Figure 1.20:** *Scheme of the Wollaston prism.*

rays are separate at the diagonal interface. There, the  $e$ -ray becomes an  $o$ -ray, changing its refractive index accordingly and vice versa. In calcite  $n_e < n_o$  so the  $e$ -ray is bent away from the normal to the interface, and the  $o$ -ray is bent toward the normal to the interface. The deviation angle between the two emerging beams is determined by the prism's wedge angle.

In Figure 1.21 the evolution of the probe polarization is shown at each step of the polarization manipulation with or without the THz field. Without the THz field the linearly polarized optical pulse passes through the crystal and remains linear, evolving into a circular polarized field after the  $\lambda/4$ , finally the Wollaston prism splits the probe beam into two orthogonal components, which are sent to the photodetectors. In this case the two components are balanced, namely of the same intensity. Instead, when the linearly polarized optical pulse and the THz pulse simultaneously propagate through the crystal, the field-induced birefringence produces a slightly elliptical polarization of the probe pulse. The probe polarization evolves into an almost circular, but slightly elliptical polarization after a  $\lambda/4$ -plate, and the two intensities are no longer balanced after the Wollaston.

What we measure is the difference between the two photodetectors, so, the

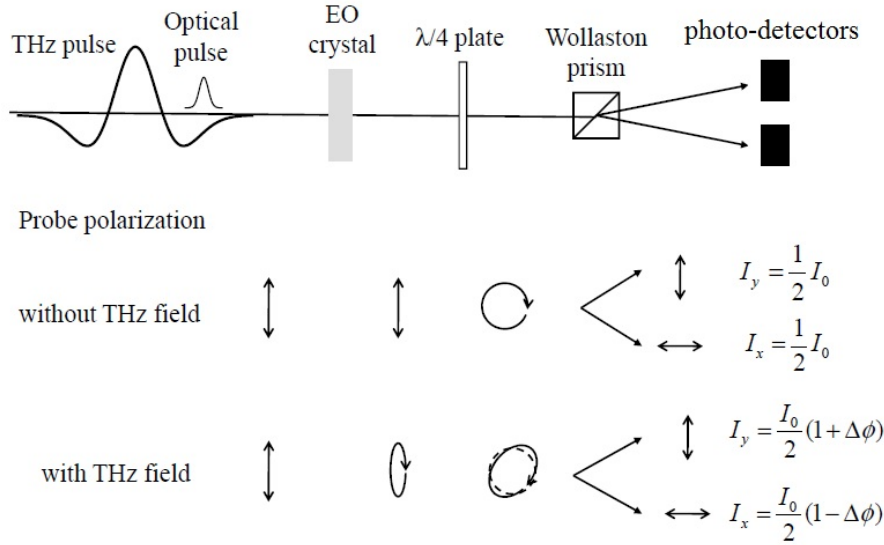


**Figure 1.21:** Probe polarizations with and without a THz field are depicted before and after the polarization optics.

difference  $I_s = I_y - I_x$  between the two orthogonal components of the probe pulse, which is proportional to the applied THz field amplitude.

The useful characteristics of ZnTe for THz generation near 800 nm are the high transparency at optical and THz frequencies and large EO coefficient ( $r_{41} = d_{14} = 4\text{pm/V}$ ) which are also desirable for efficient electro optical sampling. A typical arrangement of the optical and THz polarizations for electro optical sampling is shown in Figure 1.22. The field induced birefringence is maximized when both the THz electric field and the optical polarization are parallel to the  $[1\bar{1}0]$  axis of an  $\langle 110 \rangle$  oriented crystal. We can describe the nonlinear polarization in Eq. 1.48 as the matrix equation

$$\begin{aligned}
 \begin{pmatrix} P_x \\ P_y \\ P_z \end{pmatrix} &= 4\epsilon_0 d_{14} \begin{pmatrix} 0 & 0 & 0 & 1 & 0 & 0 \\ 0 & 0 & 0 & 0 & 1 & 0 \\ 0 & 0 & 0 & 0 & 0 & 1 \end{pmatrix} \begin{pmatrix} E_{O,x} E_{THz,x} \\ E_{O,y} E_{THz,y} \\ E_{O,z} E_{THz,z} \\ E_{O,y} E_{THz,z} + E_{O,z} E_{THz,y} \\ E_{O,z} E_{THz,x} + E_{O,x} E_{THz,z} \\ E_{O,x} E_{THz,y} + E_{O,y} E_{THz,x} \end{pmatrix} \\
 &= -4\epsilon_0 d_{14} \mathbf{E}_O E_{THz} \mathbf{e}_z \perp \mathbf{E}_O,
 \end{aligned} \tag{1.50}$$

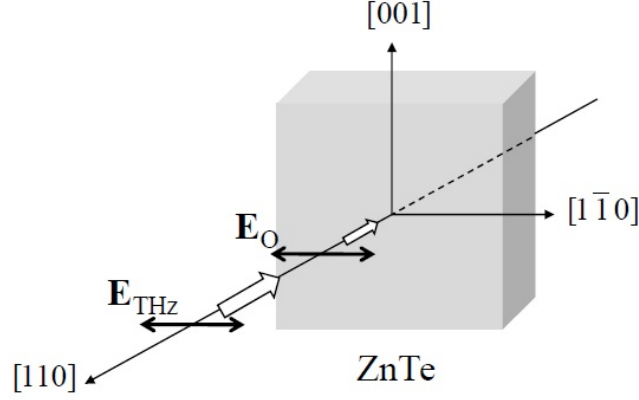


**Figure 1.22:** Polarizations of the optical probe and the THz field are parallel to the  $[1\bar{1}0]$  direction of a ZnTe crystal in a typical electro optical sampling setup.

where

$$\mathbf{E}_O = \frac{E_O}{\sqrt{2}} \begin{pmatrix} 1 \\ -1 \\ 0 \end{pmatrix} \quad \text{and} \quad \mathbf{E}_{THz} = \frac{E_{THz}}{\sqrt{2}} \begin{pmatrix} 1 \\ -1 \\ 0 \end{pmatrix}. \quad (1.51)$$

The nonlinear polarization at the optical frequency is orthogonal to the incident optical field, which implies that the linear polarization of the optical probe evolves into an elliptical polarization via propagation in ZnTe under the influence of the THz field.

The differential phase retardation  $\Delta\phi$  experienced by the probe beam due to the Pockels effect over a propagation distance  $L$  is given as [10]

$$\Delta\phi = (n_y - n_x) \frac{\omega L}{c} = \frac{\omega L}{c} n_O^3 r_{41} E_{THz}. \quad (1.52)$$

The intensities of the two probe beams at the photodetectors are

$$\begin{aligned} I_x &= \frac{I_0}{2} (1 - \sin \Delta\phi) \approx \frac{I_0}{2} (1 - \Delta\phi) \\ I_y &= \frac{I_0}{2} (1 + \sin \Delta\phi) \approx \frac{I_0}{2} (1 + \Delta\phi), \end{aligned} \quad (1.53)$$

where  $I_0$  is the incident probe intensity. For the approximation we use  $\Delta\phi \ll 1$  which is true for most cases of electro optical sampling. Thus, the difference of the intensities of the two photo-detectors is proportional to the THz field

amplitude:

$$I_s = I_y - I_x = I_0 \Delta\phi = \frac{I_0 \omega L}{c} n_O^3 r_{41} E_{THz} \propto E_{THz}. \quad (1.54)$$

# Chapter 2

## Experimental Setup

In this chapter we describe the experimental setup realized for the THz spectroscopy. The generation and in particular the detection of THz pulses is not simple and immediate. We realized a series of different setups to find the signal and further setups to improve it. Figure 2.1 shows the last setup. The laser beam at 790 nm produced by the laser source (see section

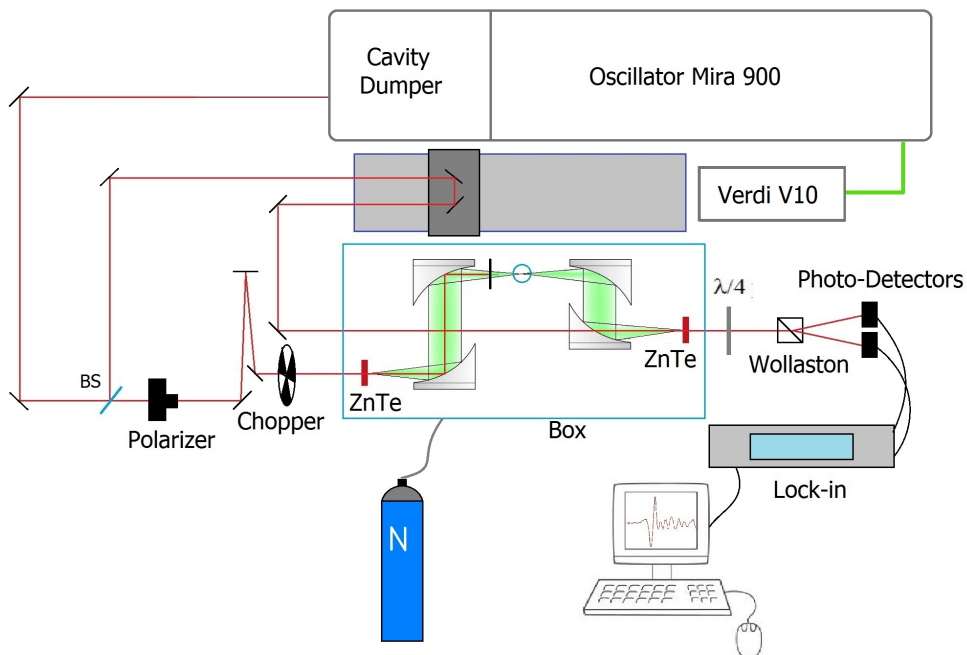


**Figure 2.1:** *Experimental setup.*

2.1) is separated by a beamsplitter 70/30%. The 70% part passes through

a polarizer preceded by a  $\lambda/2$  plate which determines the beam polarization and a chopper sets the reference frequency for the lock-in acquisition. Then, the beam is focused on the first ZnTe crystal, which is 1 mm thick and produces the THz pulses (see section 1.1). The remaining part of the 790 nm beam is stopped by a black paper that is transparent in THz range. The first golden parabolic mirror (see 2.2) parallelizes the THz beam which is focused on the sample by the second parabolic mirror; in the same way the third mirror parallelizes the beam and the fourth focuses it on the second ZnTe crystal, which is 0.5mm thick. The THz path ends in this crystal.

The 30% part of the laser beam passes on a slide which allows to change the length of optical path, then is focalized on the second ZnTe crystal passing through the fourth parabolic mirrors which has a little hole along the axis. In this way THz and optical beams are collinear and are both focused on the ZnTe crystal in spatial and temporal coincidence. In this crystal occurs the electro optic effect. The optical beam passes through the  $\lambda/4$  plate, than the Wollaston prism separates the two orthogonal components of the polarization which are detected by two detectors.

The lock-in amplifier (see section 2.5) filters the component at the difference of the two signals and sends it to a computer in which a program allows the slide control and the signal acquisition simultaneously.

A plexiglas box (see section 2.4), in which nitrogen is pumped includes totally the THz beam path.

## 2.1 Laser System

The laser system consists of three parts, which in order are: Coherent Verdi V-10, Coherent Mira 900 and Cavity Dumper APE Pulse Switch.

### Verdi V10

The Coherent Verdi V10 is the optical pump of the oscillator Coherent Mira 900. It is a solid state diode-pumped laser that provides continuum monochromatic output with a wavelength of 532 nm and a maximum power of 10 W. This laser consist of two parts: the laser head and the power supply connected by a cylindrical pipe that contains fibers and cables. A chiller

is used to cool down both the laser head and the power supply. Inside the cylindrical pipe there are fiber optics and electrical cables. The fiber optics transmit light from the diode bars in the power supply to the laser head, the electric cables provide control and monitoring signals between the two parts.

The laser head utilizes a Neodymium Vanadate (Nd:YVO<sub>4</sub>) crystal as active medium with the pump power provided by fiber delivery; this medium is a homogeneously broadened system, so the Verdi tends to naturally run at single frequency.

## Mira 900

The Coherent Mira 900 is a Ti:Sapphire oscillator. It is a mode-locked laser that produces ultra short, wide bandwidth, femtosecond pulses at a repetition rate of 76 MHz. The laser wavelength is tunable from 760 to 840 nm; we use the laser at the wavelength of about 800 nm, which gives the best results in terms of stability and pulse quality (see Figure 2.2 [13]). The pulse duration

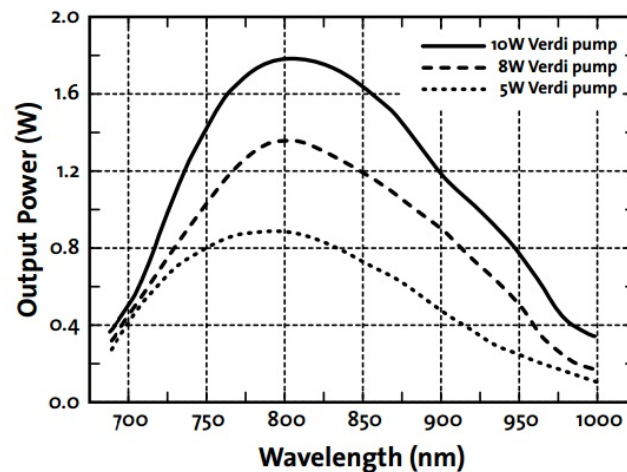


**Figure 2.2:** Output power of Mira 900 pumped by Verdi different powers in function of wavelength.

(FWHM) is of about 130 fs. The output beam has horizontal polarization. The modelocking is a method to produced these ultrashort laser pulses. The technique used to mode-lock the Laser is the *Kerr Lens Mode-Locking* which allows to induce a fixed phase difference between the cavity modes.

The Kerr-lens modelocking is a passive modelocking because the system modulates the beam through the nonlinear effects of the Ti:Sapphire crystal in cavity. The Ti:Sapphire crystal in Mira cavity is both the active medium which, pumped with Verdi V10, emits light at about 800 nm and the nonlinear crystal responsible of the Kerr-lens modelocking. In Figure 2.3 is shown this effect. Ti:Sapphire has a refractive index which depends on

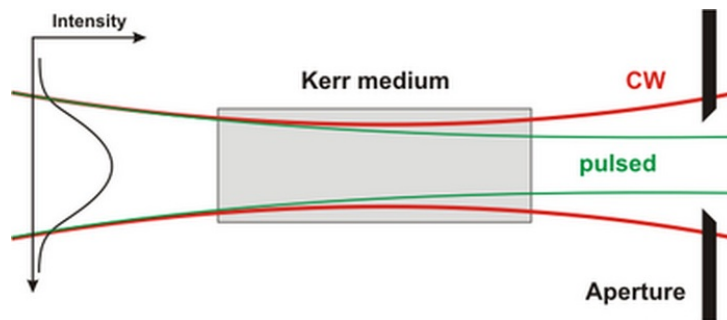


**Figure 2.3:** Scheme of Kerr lens effect with low-intensity (red line) and high intensity (green line) light.

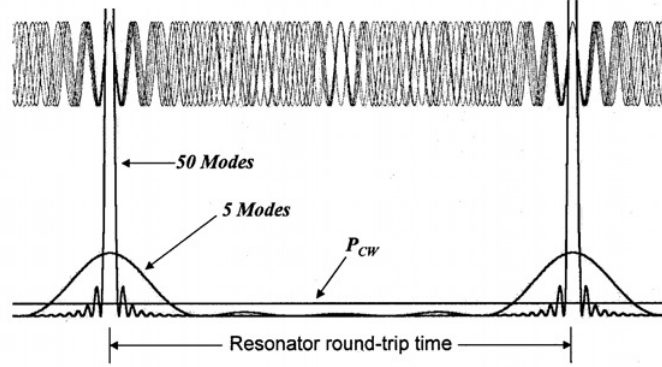
the beam intensity. In this way it is like a lens at high intensity of the field. Initially the modes change phase randomly. When they are in phase, the beam is focused and passes through the slit located after the crystal and the system stabilizes in this state which is energetically favorable. The pulsed beam is then produced.

Figure 2.4 shows an example of in phase modes interference which produces gaussian pulses. Figures 2.5a and b shows the importance of phase relations for the pulse intensity.

## Cavity Dumper

The last component of the laser system is the cavity-dumper APE Pulse Switch. It is an intra-cavity acousto-optical switch for reducing the pulse repetition rate of the mode-locked laser system. This method not only reduces the pulse repetition rate but also provides an increased output pulse energy and peak power.

This instrument is based on the acousto-optical effect for which an intensity modulation in a material generated by an acoustic wave induces a refractive index modulation of the material. The beam which passes through the crystal



**Figure 2.4:** Number of modes and increasing of pulse intensity.

is partially diffracted at an angle that depends on the modulation periodicity. The output pulses are the diffracted pulses. This effect occurs in a silica crystal setted on a piezo-electric material to which radio-frequency pulses are applied. As we can see in figure 2.6 the beam in cavity (red line) crosses the crystal which is periodically modulated by an acoustic wave and only the diffracted part (blu line) is sent out of cavity. Then the non diffracted part is not lost but stays in the cavity accumulating energy.

The cavity dumper extend the cavity length, so the repetition rate decreases from 76 MHz to 54.3 MHz. Instead in cavity dumper mode we can change the repetition rate from 27.15 MHz (one pulse every two pulses) to 200 Hz (one pulse every 260000).

The laser beam average power  $P_{av}$  in CW mode is 230 mW, so the pulse energy is

$$E_{pulse} = \frac{P_{av}}{RepRate} = \frac{230mW}{54.3MHz} = 4.2nJ \quad (2.1)$$

and the 130 fs pulses have a peak power of

$$P_{peak} = \frac{E_{pulse}}{FWHM} = \frac{4.2nJ}{130fs} = 30KW \quad (2.2)$$

In our measurement we set the division rate at 100, consequently the repetition rate is 543 KHz and the average power  $P_{av}$  is about 20 mW. The

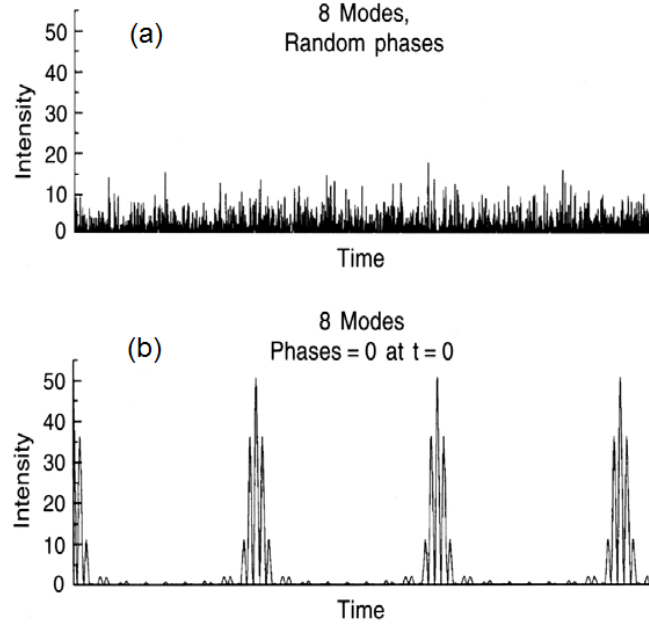


**Figure 2.5:** a) 8 modes with casual phase, b) 8 modes with the same phase.

pulse energy and the peak power are then

$$E_{pulse} = \frac{20mW}{543KHz} = 36.8nJ \quad (2.3)$$

$$P_{peak} = \frac{36.8nJ}{130fs} = 0.28MW \quad (2.4)$$

and comparing these equation with equations 2.1 and 2.2 it is clear the energy and peak power gain.

## Oscilloscope

The laser pulses described in this section are visible on the oscilloscope connected to the laser system with BNC cables. On the oscilloscope display (Figure 2.7) we can see the comb of pulses at 54.3 MHz (light blu line). In correspondence of an acoustic pulse of the cavity dumper (yellow line) there is an energy loss of cavity pulses because of the emission of one pulse. During time  $\tau$  the energy increases and returns to the maximum value. This time  $\tau$  sets the smallest time between two consecutive acoustic pulses; in practice we have to permit that the system recovers energy.

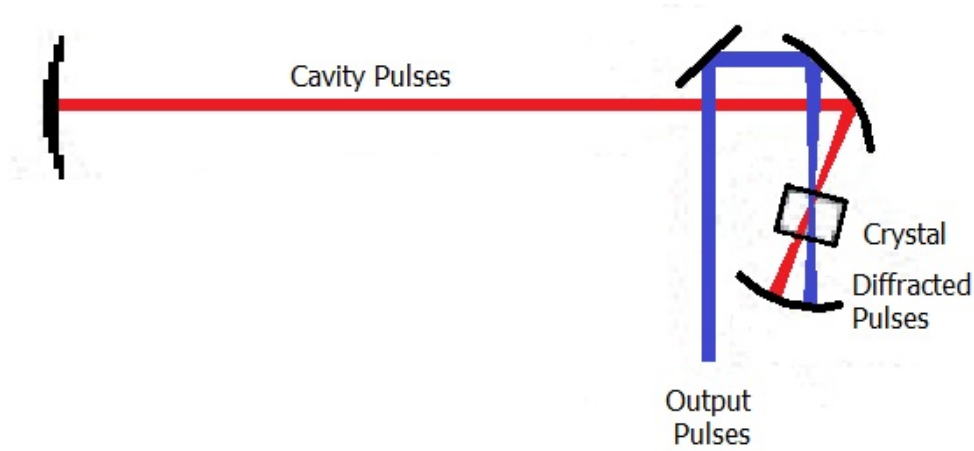


**Figure 2.6:** *Scheme of cavity dumper.*

## 2.2 Parabolic Mirrors

To lead the THz beam we use four  $90^\circ$  off-axis parabolic mirrors with a protected gold coating. In Figure 2.8a is shown the mirror scheme. The diameter is 50.8 mm, thickness 62.8 mm, reflected focal length 101.6 mm and parent focal length 50.8 mm.

We use parabolic mirrors because they have no spherical or chromatic aberration and their large area allows to collect more THz wave. The last parabolic mirrors has a little hole of about 5 mm diameter located as in Figure 2.2b in order to have the optical and THz beams collinear and then focalized on ZnTe crystal.

## 2.3 $\lambda/2$ Plate and Polarizer

The  $\lambda/2$  Plate and Polarizer are located on the THz line before the THz generation. The aim of these two components is to change the polarization of the 800 nm beam in order to maximize the generation process (see Section 1.1.7). The polarizer is an optical device which selects the linear polarization of the output light. If the input light with field amplitude  $E_0$  is linearly polarized, only the component of the optical field parallel to the transmission axis passes through the device. Then the output beam is linearly polarized



**Figure 2.7:** A photograph of oscilloscope display.

along the polarizer transmission axis with amplitude

$$E_{out} = E_0 \cos \theta \quad (2.5)$$

where  $\theta$  is the angle between the polarization direction of the input beam and the polarizer axis. The intensity then depends on  $\theta$

$$I(\theta) = I(0) \cos^2 \theta \quad (2.6)$$

which is the Malus's Law.

The  $\lambda/2$  plate is an optical device which shifts the polarization direction of linearly polarized light. It is a birefringent material, for which the refractive index is different for different orientations of light passing through it. The plate introduces a relative phase difference of  $\pi$  between the crystal fast axis and slow axis. With this mechanism the  $\lambda/2$  plate is a polarization rotator. The incident polarization direction is then rotated depending on the direction of the crystal axes. Rotating the crystal we can switch the incident linear polarization to all possible directions.

Coupling the  $\lambda/2$  plate with the polarizer we can have the maximum intensity for all output polarization directions.

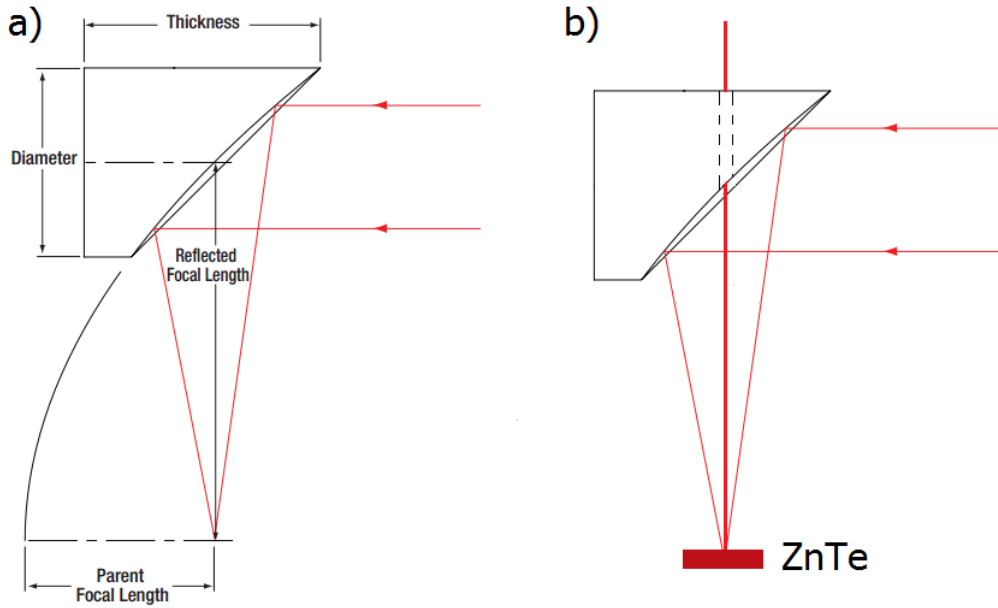


Figure 2.8: Scheme of parabolic mirror.

## 2.4 THz Box

Water vapour, oxygen molecules and other air components have absorption in THz range. This problem is solved by the THz box that is a simple box composed of  $5\text{mm}$  thick plexiglas sheets which contains the THz beam from the generation crystal to the detection crystal. In this box we pump nitrogen gas with the aim of sending out the THz absorbing air components.

## 2.5 Lock-in Amplifier

The lock-in amplifier is the Signal Recovery 7265. The basic idea of this instrument is the detection of signals modulated at the reference frequency  $\omega_r$ . This instrument allows to detect very small signals. The technique used to single out the component of the signal at a specific reference frequency is known as phase-sensitive detection. Noise at frequencies other than the reference frequency are filtered out and don't affect the measurements. In our case this frequency is 3 KHz and it is the chopper frequency which is transmitted to the lock-in by a BNC cable. The signal that enters the lock-in can be written as  $V_{sig} \sin(\omega_r t + \phi_{sig})$  where  $V_{sig}$  is the signal amplitude. The

lock-in generates its own sine wave that can be called lock-in reference and has the form  $V_L \sin(\omega_L t + \phi_L)$ . The signal is amplified and multiplied by the lock-in reference using a phase-sensitive detector (PSD) or multiplier. The output of the PSD is simply the product of two sine waves:

$$\begin{aligned} V_{psd} &= V_{sig} V_L \sin(\omega_r t + \phi_{sig}) \sin(\omega_L t + \phi_L) \\ &= \frac{1}{2} V_{sig} V_L \cos[(\omega_r - \omega_L)t + \phi_{sig} - \phi_L] + \\ &\quad - \frac{1}{2} V_{sig} V_L \cos[(\omega_r + \omega_L)t + \phi_{sig} + \phi_L] \end{aligned} \quad (2.7)$$

The PSD output is formed by two AC signals, one at the difference frequency  $(\omega_r - \omega_L)$  and the other at the sum frequency  $(\omega_r + \omega_L)$ . The output is filtered through a low pass filter in order to remove the AC signals, then the only signal surviving is the difference frequency component. We set the lock-in frequency the same as the signal frequency  $(\omega_L = \omega_r)$ , so the filtered PSD output is

$$V_{psd} = \frac{1}{2} V_{sig} V_L \cos(\phi_{sig} - \phi_L) \quad (2.8)$$

which is a DC signal proportional to the signal amplitude. The PSD and low pass filter detect only signals whose frequencies are very close to the lock-in reference frequency. Only the signal at the reference frequency will result in a true DC output and be unaffected by the low pass filter: this is the signal to be measured. We observe that in order to have a DC signal in PSD output, the phase difference between the two signals cannot change in time.

The PSD output is then proportional to  $V_{sig} \cos \phi$  where  $\phi = \phi_{sig} - \phi_L$ . This phase dependence can be eliminated by adding a second PSD which multiplies the signal with the reference oscillator shifted by  $90^\circ$ , i.e.  $V_L \sin(\omega_L t + \phi_L + \pi/2)$ . Its low pass filtered output will be

$$V_{psd2} = \frac{1}{2} V_{sig} V_L \sin(\phi_{sig} - \phi_L), \quad (2.9)$$

then proportional to  $V_{sig} \sin \phi$ . So there are two outputs, one is proportional to  $\cos \phi$  and the other to  $\sin \phi$ . We call  $X$  and  $Y$  respectively these two outputs:

$$X = V_{sig} \cos \phi \qquad Y = V_{sig} \sin \phi. \quad (2.10)$$

The phase dependency is removed by computing the magnitude  $R$  of the signal vector, which results

$$R = \sqrt{X^2 + Y^2}. \quad (2.11)$$

## 2.6 Acquisition System

The two photo-detectors *Thorlabs DET210* are high-speed silicon detectors which send the two signals to the two lock-in inputs A and B. They are both terminated with a 180 K $\Omega$  resistance to increase the integration time. Figure

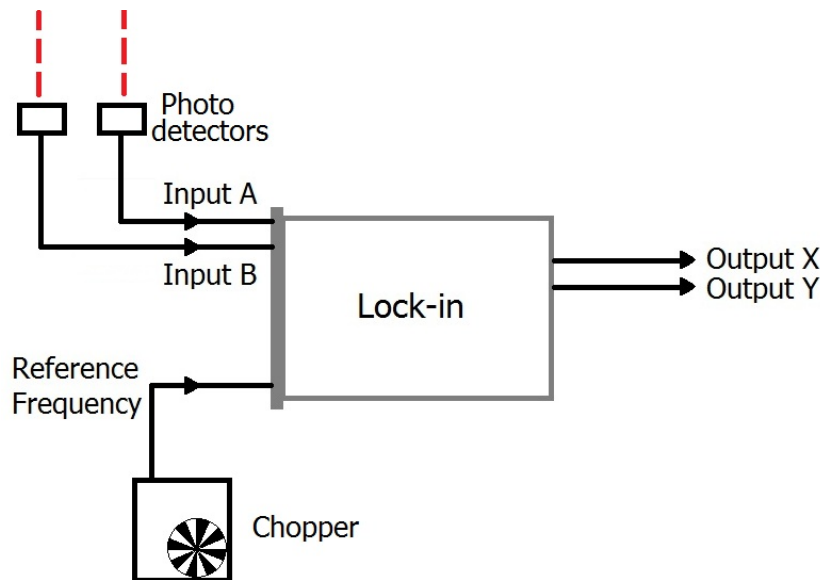


**Figure 2.9:** Lock-in image and scheme.

2.9 shows the lock-in acquisition scheme.

The lock-in input signal is the difference A-B of the two inputs and the reference frequency is the chopper frequency. The lock-in sensitivity is set to 0.2 mV and a good integration time for our measurements is from 10 to 500 ms. The  $X$  and  $Y$  signal of the A-B difference are sent to the acquisition device *National Instruments PCIe-6251* which converts the analog signals to digital signals. Finally the Labview program shown in figure 2.10 allows the control of signal acquisition parameters and slide movement. As we can see in the left panel the program allows the choice of the scan length in  $\mu\text{m}$  and

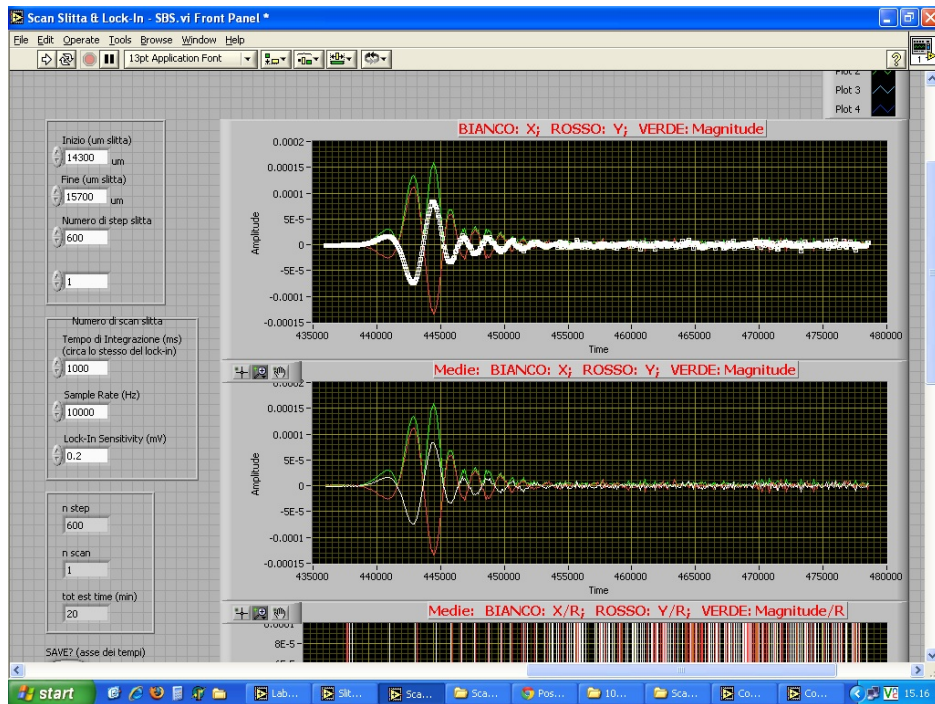


Figure 2.10: The acquisition Labview program.

the number of steps. Furthermore is possible to make more than one scan: the first graph shows the real time data and the second graph shows the final result that is an average of all scans. The two graphs show three lines, the red and white line are the  $X$  and  $Y$  signals and the green line is the  $R$ .

# Chapter 3

## Experimental Results

In this chapter we present and discuss the THz measurements. We first show how to find the THz signal and the maximization procedure with the comparison between the experimental data and the theoretical analysis of chapter 1. Then we present the THz signal acquired in air and the signal in Nitrogen exploiting the THz box described in section 2.4. Finally we highlight the high phase sensitivity of these measurements due to the fact that with the electro optical sampling technique we measure directly the electric field of the THz pulses.

### 3.1 Signal Acquisition and Optimization

Finding the THz signal is not straightforward because there are a lot of degrees of freedom that must be controlled.

The main issue is the spatial and temporal coincidence of the THz and optical beams in the ZnTe crystal for electro-optical sampling.

To find the spatial coincidence we exploit the residual 800 nm beam which remains from the generation process in the first ZnTe crystal. This 800 nm beam is collinear to the THz, so, in order to find the spatial coincidence. In this way we can align correctly and easily the four parabolic mirrors to have the two 800 nm beams collinear after the last parabolic mirror. Once set the two beams collinear, it is now simple to find the spatial coincidence in the last crystal replacing it with a little pinhole of about 75 or 50  $\mu\text{m}$ .

As we can see in Figure 3.1, the optical sampling beam is focused with a

20 cm lens located before the fourth parabolic mirror and the other two collinear beams are focused by the same mirror. In order to have the same

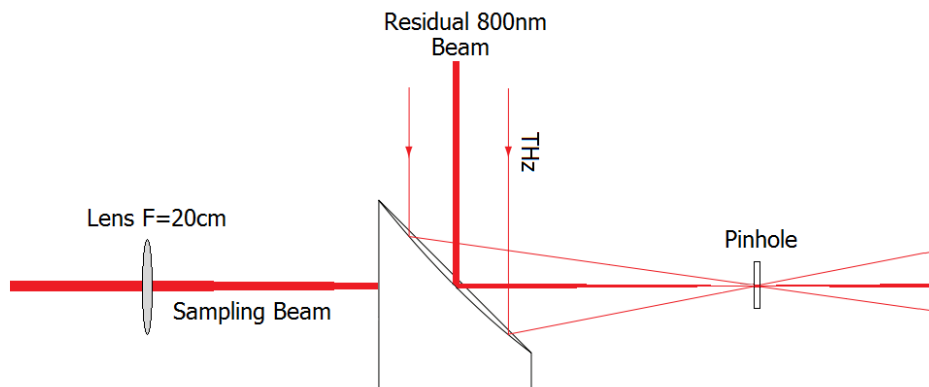


**Figure 3.1:** *Scheme of the beams alignment.*

focus point we first put the pinhole in the mirror focus maximizing the output light. Then we move the sampling beam focus translating the 20 cm lens to set it exactly in the mirror focus point. When both the 800 nm beams pass through the pinhole, the spatial coincidence is achieved and we can so replace the pinhole with the ZnTe crystal.

The temporal coincidence of THz and optical beams in the ZnTe crystal is the fundamental point for the electro optical sampling. Temporal coincidence means that the two pulses have to be in the crystal in the same time, then they can interact each other. To do that the two optical paths from the beam-splitter to the last ZnTe crystal must be the same.

In practice we replace the ZnTe crystal with a BBO crystal. The BBO crystal is a nonlinear crystal which is a second-harmonic generator for the 800 nm beams. This crystal has in input the 800 nm sampling beam and the other 800 nm beam collinear with the THz. As outputs there are the two second harmonics of the two 800 nm beams and, only if the temporal coincidence is satisfied, the sum frequency beam. These three output have the same wavelength at 400 nm and they are now collinear, so indistinguishable. To see the sum frequency spot, which is the temporal coincidence indicator, we can create a little divergence between the two beams but always maintaining the spatial coincidence with the pinhole aid. In this way, for the momentum conservation, in temporal coincidence conditions we

can see the sum frequency spot between the other two beams (Figure 3.2). To find this spot we can simply move the mechanical slide that varies the

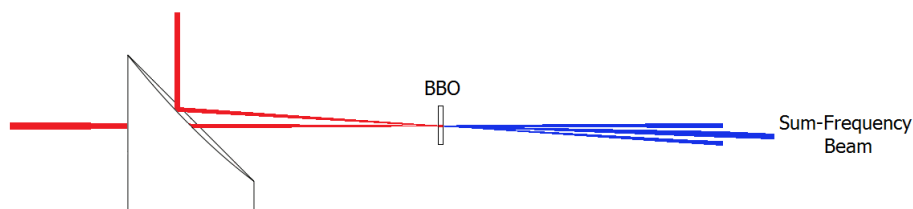


**Figure 3.2:** *Sum frequency generation in temporal coincidence conditions.*

sampling beam optical path, until the sum frequency spot appears.

Since we are in spatial coincidence and we know the slide position which satisfies the temporal coincidence, we can start the acquisition process moving the slide around this point. The run starts few hundred micrometer before and finishes few hundred micrometers after the coincidence point. In Figure 3.3 is shown the pulse acquired in air with a  $700\ \mu\text{m}$  run slide, 100 steps and a lock-in integration time of 200 ms. In the two graphs is shown

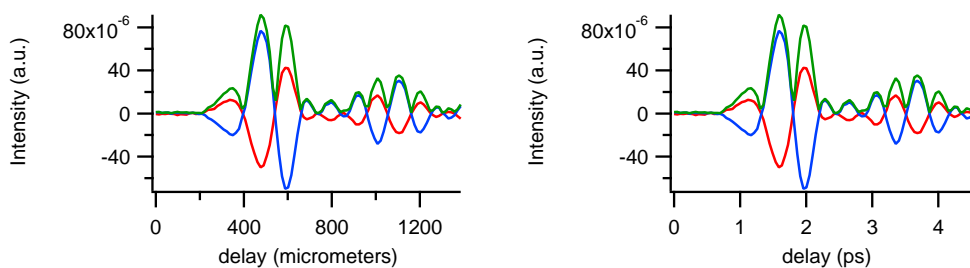


**Figure 3.3:** *THz signals in space and time. X (red line), Y (blue line), R (green line)*

the same pulse, the difference is the x-axis. The right graph x-axis is the slide delay in picoseconds, the left graph x-axis in micrometers. We underline the fact that beam crosses the slide two times, then, since the slide range is of  $700\ \mu\text{m}$ , the space axis is of  $1400\ \mu\text{m}$ .

Once found the THz signal we have to optimize all the parameters to have the maximal THz signal. We get in the maximum of  $R$  and we change

the crystals angles and beams polarization maximizing the  $R$  value in the lock-in display. While changing angles and polarization we have to consider the theoretical analysis of section 1.1.7. We report in the graphs of Figure 3.4 the two main results of the THz generation analysis. In the detection

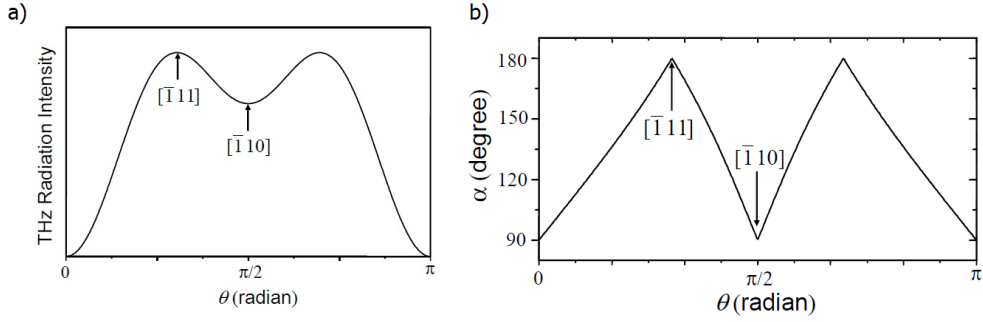


**Figure 3.4:** a) THz radiation intensity vs  $\theta$ , b) Angle between the optical and the THz field as a function of  $\theta$ .

crystal the signal is maximized when the THz beam and sampling beam are parallel to the  $[\bar{1}10]$  crystal axis. Measuring separately the three effects is rather difficult because we have to control simultaneously the polarization of the three beams and the angle of the two crystals. What we made is varying only the generation crystal angle between  $-\pi/2$  and  $\pi/2$  acquiring the  $R$  value. Then the only polarization that changes is the THz polarization. The others are fixed: the sampling beam is horizontally polarized and the other 800 nm beam is vertically polarized. We show the data in Figure 3.5a. We

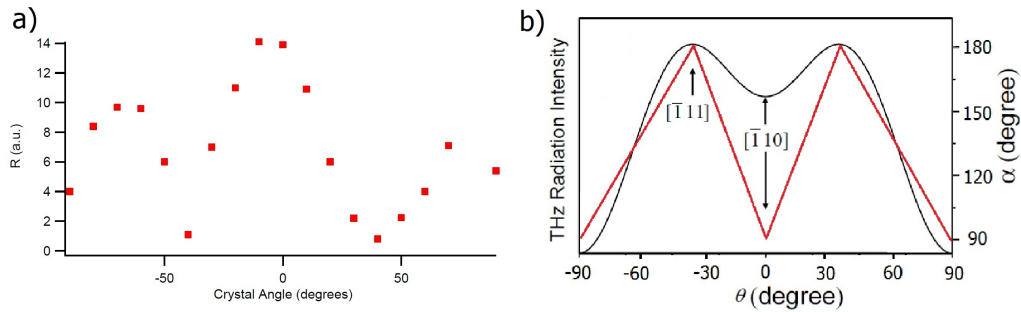


**Figure 3.5:** a)  $R$  at pulse maximum in function of the generation crystal angle, b) Radiation intensity and  $\alpha$  angle vs  $\theta$ .

now try to disentangle the three effects in this figure. To better explain

this mechanism we reported in Figure 3.5b the two effects of Figure 3.4 in a single graph and we change the x-axis between  $-90$  and  $90^\circ$ . First we note that the graph has a high symmetry due to the fact that all three effects are symmetric. In  $\theta = 0^\circ$  there is the maximum intensity. The  $\alpha$  angle indicates that the THz and sampling beam have the same polarization (horizontal), so the detection is maximized. The THz intensity is in a relative minimum but is still high. In  $\theta \sim \pm 40^\circ$  the intensity has two minima because, although the THz intensity is maximal, its polarization is perpendicular to the sampling beam polarization and the detection process is not efficient. In  $\theta \sim \pm 70^\circ$  we see two relative maxima. In this case the THz polarization is at about  $45^\circ$  from the other and the THz intensity is at about half maximum. Finally at  $\theta \sim \pm 90^\circ$  the detected intensity tends to zero because of the intensity of the THz pulses. In fact, although the two polarization are again parallel, the generation process is not efficient.

## 3.2 In Air Measurements

In this section we present the THz measurements in air, without sample. The THz band shows high atmospheric opacity due to the rotational lines of constituent molecules. The air contains roughly 78.09% nitrogen, 20.95% oxygen, 0.93% argon, 0.039% carbon dioxide, and small amounts of other gases. It also contains a variable amount of water vapour, on average around 1%. In Figure 3.6 the THz pulse after free propagation in air is shown. As we can see in the first graph the result is a confused time-domain trace with many absorption lines in its spectrum (second graph), which is in logarithmic scale. The long time oscillations in time-domain and the peaks in the frequency-domain pulse are caused by absorption and re-radiation from molecules in air, which have resonances in the THz region [14]. The absorption by water vapour is the predominant process of air THz attenuation. We can see in Figure 3.7 the water vapour transmission spectrum from 0.3 to 6 THz [3]. In order to compare this spectrum with the THz spectrum of figure 3.6 we overlap the two graphs in Figure 3.8. The figures 3.8a and b are the same spectra in different range. The first is between 0 to 4 THz and the second between 0.5 to 2 THz. The comparison between the two spectra is immediate, in particular in the Figure 3.8b. In fact there are five indicated

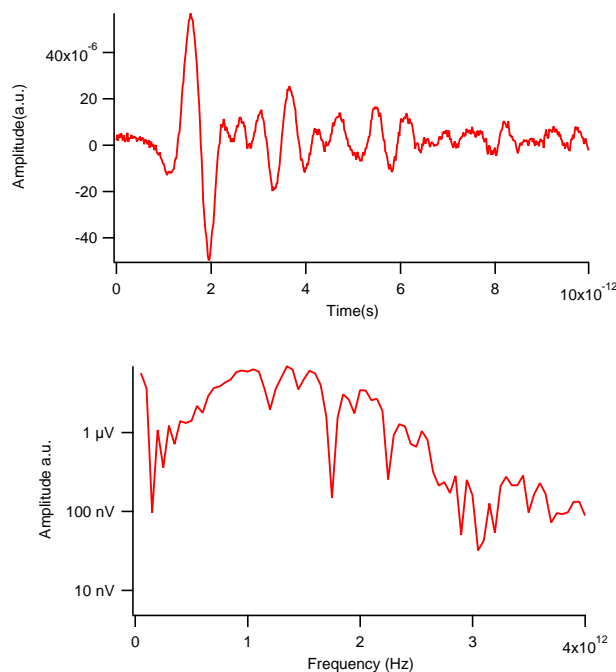


**Figure 3.6:** *In-air THz pulse and its Fourier transform.*

evident peaks in THz spectrum corresponding to different lines of the water vapour absorption spectrum. We can see that also the intensities of the peaks correspond. The most intense and large peak (4) includes the two higher peaks of water absorption spectrum at 1.66 and 1.72 THz and other three small peaks at 1.6, 1.76 and 1.8 THz. The effect of this three peaks is visible in the shape of the spectrum peaks at the corresponding frequencies. The second peak (2) corresponds to five water peaks between 1.1 and 1.25 THz. The last peak (5) corresponds to two peaks at 1.87 and 1.92 THz and the others ((1),(3)) correspond to a single and low intensity peak. We can see in Figure 3.8a that also after 2 THz there is a good agreement between the two spectra.

### 3.3 In Nitrogen Measurements

There are two main options to clean up the spectrum removing the water vapour absorption lines. The first is to place the THz apparatus inside a vacuum chamber, excluding the  $\lambda/4$  plate, Wollaston prism, and the two

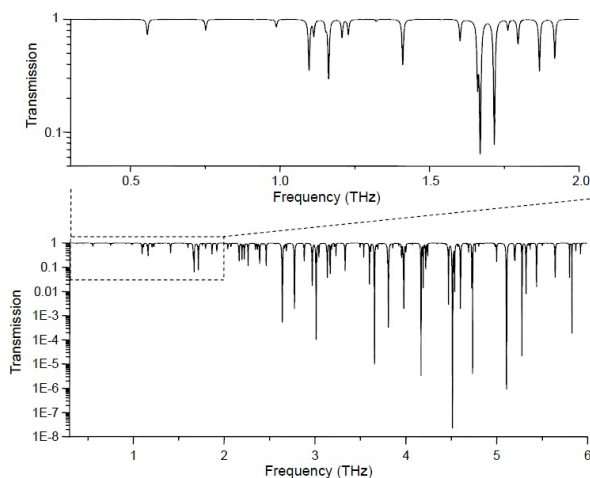


**Figure 3.7:** *Water vapour transmission spectrum from 0.3 to 6 THz.*

detectors. The second option is the THz box described in section 2.4. In this plexiglas box we pump nitrogen gas with the aim of creating an over pressure of  $N_2$  and send out the water vapour molecules.

The resulting THz pulse and its spectrum in logarithmic scale is shown in Figure 3.9. The oscillations after the THz pulse are removed, leaving only the rectified THz field. The spectrum is significantly cleaner and there is no trace of the water vapour absorption peaks. The frequency range for THz spectroscopy is from 0.5 to 2.5 THz. We can compare the in-air and in-nitrogen spectra in Figure 3.10 where we show the two spectra in logarithmic and linear scale. In both these spectra we can see that the spectral content of the pulse decreases rapidly at about 2.5 THz. This behaviour is due to the absorption of ZnTe crystal. In fact, as discussed in section 1.1.6, there is a dominant THz absorption processes in ZnTe crystals related to a strong transverse-optical (TO) phonon at  $\nu = 5.32THz$  at room temperature. We show in Figure 3.11 the absorption coefficient of ZnTe.

### 3.4 The Axes Problem

The THz electric field is reconstructed acquiring the X, Y and R signals as a function of the delay between the THz and sampling beam. The first problem is to set the time axis correctly in order to have the pulse in time domain. To

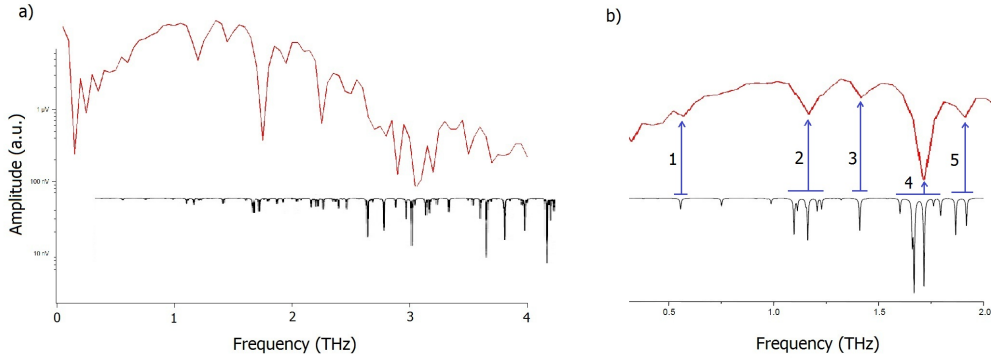


**Figure 3.8:** *Superposition of water vapour transmission spectrum and our THz spectrum in air.*

do this we have to know the slide parameters of acquisition: the run length and the number of steps which is the number of acquired points. We have to consider that the beam passes two times along the slide, so the real beam path is double the run length. With this informations we simply calculate how long is a single step dividing the double run length for the number of steps. Attributing to each acquisition point the exact length, we have the space axis. To obtain the time axis we can simply transform the space length in time length dividing by  $c$ .

For the Fourier transform we have to find the correct frequency axis. From known slide parameters we can calculate the minimum and maximum frequency detectable in the measurements. The temporal distance  $dt$  between two consecutive points sets the maximum frequency:  $\nu_{max} = 1/2dt$ , and the minimum frequency is setted by the acquired temporal window  $T$ :  $\nu_{min} = 1/2T$ . The frequency range is then  $\delta\nu = \nu_{max} - \nu_{min}$ . Dividing  $\delta\nu$  by the number of points we find the frequency  $d\nu$  of two consecutive points:  $d\nu = \delta\nu/points$ . Now the correct frequency axis starts with the minimum frequency  $\nu_{min}$  and increases with a  $d\nu$  frequency per point.

### 3.5 High Phase Sensitivity

As we already discussed. through the electro optical sampling we directly measure the THz pulse electric field, than we can directly measure the

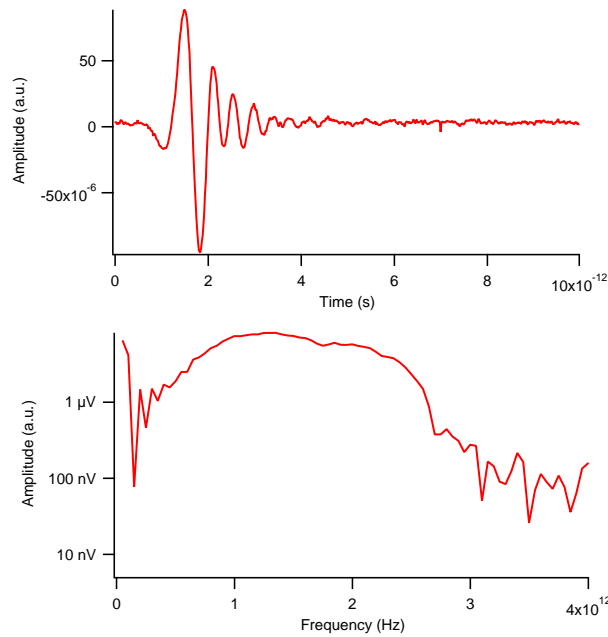


**Figure 3.9:** *In-nitrogen THz pulse and its Fourier transform.*

amplitude and the phase of the field. To show this phase sensitivity we performed measurements with paper sheets samples because they are transparent in THz range. We show in Figure 3.12 eleven in-air measurements made with 0 to 10 paper sheets. Each pulse has an offset that separates the different pulses. We can see that the temporal shift of two consecutive pulses which differs of a single paper sheet is visible and is about  $0.13\text{ps}$ .

As expected there is a linear dependence between shift and number of sheets which have the same thickness as we can see in Figure 3.13.

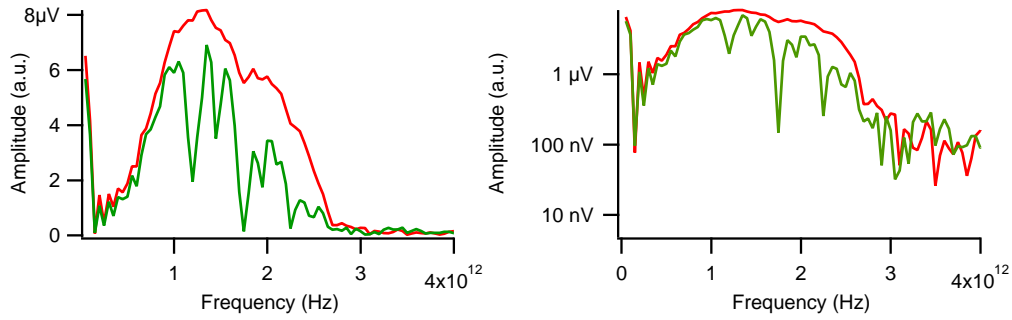


**Figure 3.10:** *In-air (green line) and in-nitrogen (red line) spectra in linear scale (right) and logarithmic scale (left).*

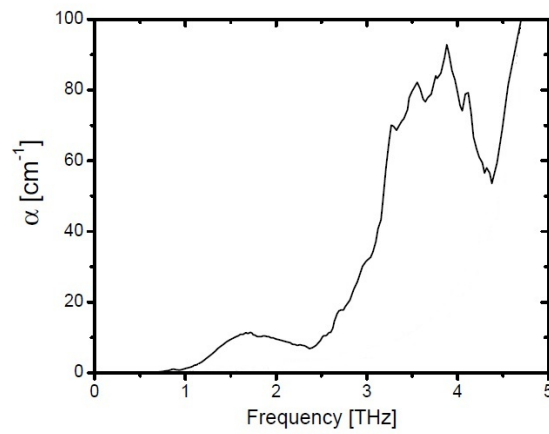


**Figure 3.11:** *Absorption of ZnTe crystal in THz range due to the transverse-optical phonon.*

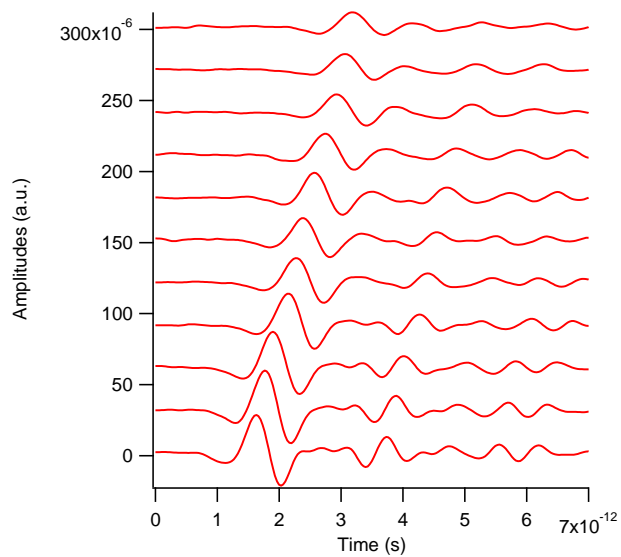


**Figure 3.12:** *In-air measurements from 0 to 10 paper sheets.*

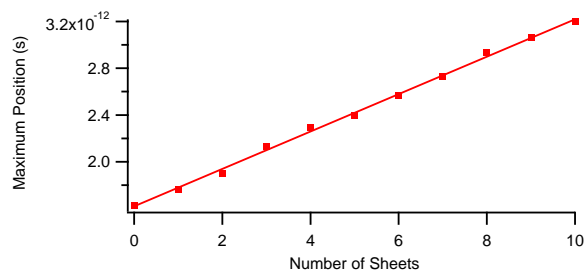


**Figure 3.13:** *In-air and in-nitrogen spectra.*

# Chapter 4

## Determination of Optical Properties

The power of THz time domain spectroscopy is the ability to record both amplitude and phase information by direct measurement of the electric field. This provides amplitude and phase information on the transmission coefficients of the sample of interest, which in turn yields both real and imaginary parts of the complex optical constants. In fact we know that the optical properties of a medium are described by the dielectric constant  $\tilde{\epsilon}$  the optical conductivity  $\tilde{\sigma}$  and the complex refractive index  $\tilde{n}$ :

$$\tilde{\epsilon}(\omega) = \epsilon_1(\omega) + i\epsilon_2(\omega) \quad (4.1)$$

$$\tilde{\sigma}(\omega) = \sigma_1(\omega) + i\sigma_2(\omega) \quad (4.2)$$

$$\tilde{n}(\omega) = n(\omega) + ik(\omega). \quad (4.3)$$

We know also that this quantities are all connected, in fact we can have the dielectric function from the refractive index with the relation:

$$\tilde{\epsilon}(\omega) = [\tilde{n}(\omega)]^2 \quad (4.4)$$

and the real and imaginary part of complex conductivity from

$$\sigma_1(\omega) = -\omega\epsilon_0\epsilon_2(\omega), \quad (4.5)$$

$$\sigma_2(\omega) = \epsilon_0\omega[\epsilon_1(\omega) - 1]. \quad (4.6)$$

We now present a procedure to obtain the complex refractive index of a medium from THz measurements. We make two THz measurements, one

with sample and the other, that is the reference, without the sample. So we have the THz pulse with sample  $E_s(t)$  and the reference pulse  $E_0(t)$ , in time-domain, and their Fourier transform:

$$E_s(\omega) = |E_s(\omega)|e^{i\phi_s(\omega)} \quad (4.7)$$

$$E_0(\omega) = |E_0(\omega)|e^{i\phi_0(\omega)}, \quad (4.8)$$

By dividing these two equations we have

$$\frac{E_s(\omega)}{E_0(\omega)} = \frac{|E_s(\omega)|}{|E_0(\omega)|}e^{i(\phi_s(\omega)-\phi_0(\omega))} = \frac{|E_s(\omega)|}{|E_0(\omega)|}e^{i\Delta\phi}. \quad (4.9)$$

We know that

$$E_s(\omega) = E_0(\omega)t_1t_2e^{i\Delta\tilde{n}(\omega)\frac{\omega d}{c}} \quad (4.10)$$

where  $d$  is the sample thickness,  $c$  the speed of light,  $\Delta\tilde{n}(\omega) = \tilde{n}_s - \tilde{n}_{air}$  and  $t_1$  and  $t_2$  are the Fresnell factors of the two interfaces (air-paper and paper-air). The expression of these two factors is:

$$t_1t_2 = \frac{4\tilde{n}_{air}\tilde{n}_{paper}}{(\tilde{n}_{air} + \tilde{n}_{paper})^2}, \quad (4.11)$$

but it is also a good approximation consider only the real part of  $\tilde{n}$ . Substituting equation 4.10 into equation 4.9 we have

$$t_1t_2e^{i\Delta\tilde{n}(\omega)\frac{\omega d}{c}} = t_1t_2e^{i(n_s(\omega)-n_{air}(\omega))\frac{\omega d}{c}}e^{-k_s(\omega)-k_{air}(\omega)}\frac{|E_s(\omega)|}{|E_0(\omega)|}e^{i\Delta\phi}. \quad (4.12)$$

If we consider  $k_{air} = 0$  and  $n_{air} = 1$  the equation becomes

$$\frac{|E_s(\omega)|}{|E_0(\omega)|}e^{i\Delta\phi} = t_1t_2e^{-k_s(\omega)\frac{\omega d}{c}}e^{i(n_s(\omega)-1)\frac{\omega d}{c}}, \quad (4.13)$$

then we have

$$\frac{|E_s(\omega)|}{|E_0(\omega)|} = t_1t_2e^{-k_s(\omega)\frac{\omega d}{c}} \quad (4.14)$$

$$\Delta\phi = (n_s(\omega) - 1)\frac{\omega d}{c}. \quad (4.15)$$

And we can find straightforwardly the  $n_s(\omega)$  and  $k_s(\omega)$ :

$$n_s(\omega) = \Delta\phi\frac{c}{\omega d} + 1 \quad (4.16)$$

$$k_s(\omega) = -\frac{c}{\omega d}\ln\left(\frac{|E_s(\omega)|}{|E_0(\omega)|}\frac{(1+n_s(\omega))^2}{4n_s(\omega)}\right). \quad (4.17)$$

In this simple treatment we showed the power of the THz time domain spectroscopy, in fact we obtained the real and imaginary parts of the refractive index of an arbitrary sample only by a THz measurements.

It is possible also find the absorption coefficient  $\alpha(\omega)$  which is defined by the following equation:

$$\frac{I_s}{I_0} = t_1 t_2 e^{-\alpha d}, \quad (4.18)$$

where  $I_s$  and  $I_0$  are the two intensities. Then,

$$\alpha(\omega) = -\frac{2}{d} \ln \left( \frac{|E_s(\omega)|}{|E_0(\omega)|} \frac{1}{t_1 t_2} \right) \quad (4.19)$$

because  $I(\omega) = |E_{\omega}|^2$ .

## 4.1 Paper Refractive Index

In this section we propose an example to understand the above explained procedure. We take the data of section 3.5 i.e. eleven different measurements from zero to ten paper-sheet, and we try to find out the paper refractive index.

We consider the measurement with one paper sheet and the reference with no sample. In Figure 4.1 we show these two pulses in time and frequency domain and the two phases. This graphs contain all the information we need to find the complex refractive index.

To determine the refractive index real part  $n_{paper}(\omega)$ , as we can see in equation 4.16, we only have to find the phase difference in function of frequency that straightforwardly follows from the phases graph in Figure 4.1. Inserting this result in equation 4.16 with the sample thickness  $d = 0,1$  mm we find the  $n_{paper}(\omega)$  function shown in Figure 4.2. This result is in total agreement with experimental data in literature [15] [16] and the Clausius-Mossotti model [15]. In fact, from 0.5 to 1 THz the refractive index decreases from about 0.5 to 0.4, than is stable at  $0.4 \pm 0.05$  until 2.5 THz.

To determine the imaginary part  $k_{paper}(\omega)$  of the refractive index we simply divide the two magnitude spectra  $\frac{|E_s(\omega)|}{|E_0(\omega)|}$  of Figure 4.1b) and we insert this result in equation 4.17 with the thickness of one paper sheet  $d = 0,1$  mm. In Figure 4.3 we show the  $k_{paper}(\omega)$  result. Loss of terahertz waves is due to scattering by the cellulose fibers [15]. We can see that in the frequency range

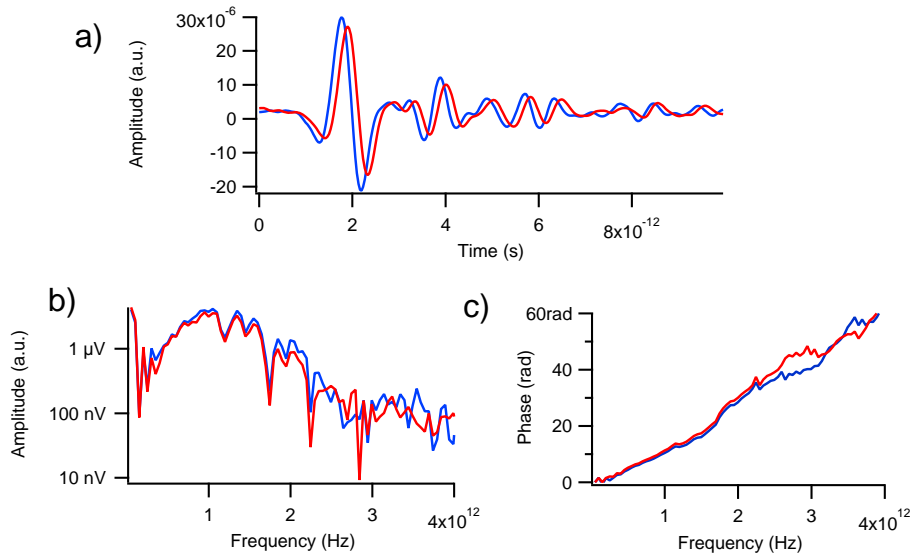


**Figure 4.1:** THz pulse with 1 paper sheet (red line) and the reference pulse (blue line). a) Pulses in time domain. b) Pulses in frequency domain c) Phases of two pulses.

of 0.5 to 2.5 THz there is a little absorption increasing [15] and the values of  $k$  oscillates between 0 and about 0.15.

From  $k(\omega)$  function we obtain the absorption coefficient defined in equation 4.19. In Figure 4.4 we show the absorption function from 0.5 THz to about 2 THz. Also this result matches with literature results [15].

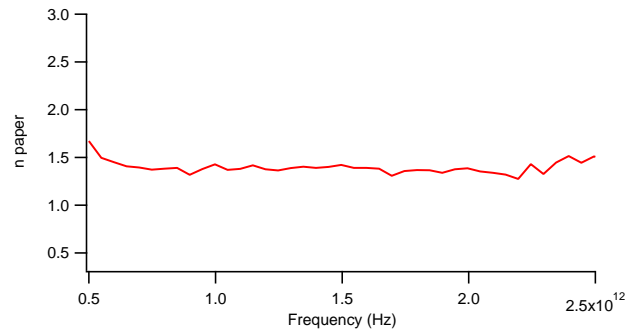


**Figure 4.2:** Refractive index imaginary part  $n_{paper}(\omega)$  determined only by THz measurements.

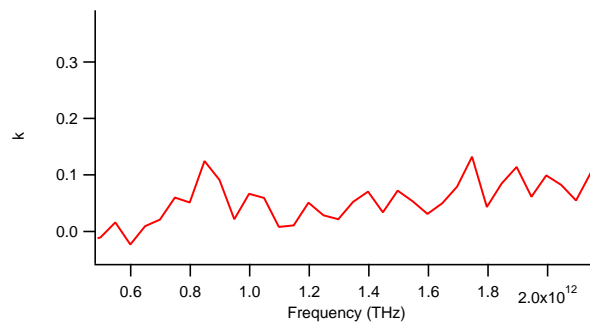


**Figure 4.3:** Refractive index real part  $k_{paper}(\omega)$  determined only by THz measurements.

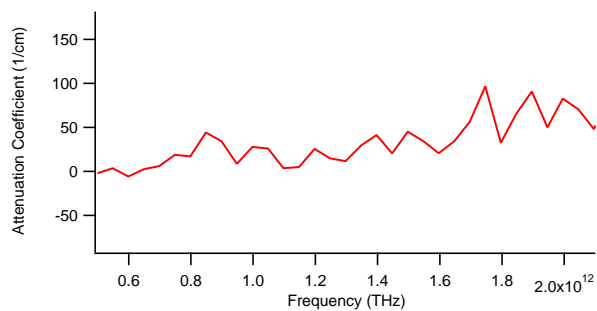


**Figure 4.4:** Absorption coefficient of paper from 0.5 to 2 THz.

# Chapter 5

## THz Time-Domain Spectroscopy Measurements

In this chapter we present and discuss some THz measurements at room temperature. We start with a  $\text{CuGeO}_3$  crystal, then we consider the organic-inorganic hybrid  $(\text{C}_6\text{H}_5\text{CH}_2\text{CH}_2\text{NH}_3)_2\text{CuCl}_4(\text{PEACuCl})$  and we conclude with sucrose and blood measurements. Some of these measurements have been performed on the THz setup of the Optical Condensed Matter Science research group of the University of Groningen, the Netherlands, which is identical to that described in section 2 for the generation and detection processes, while it differs in the laser source, that is an amplified system at 1 kHz repetition rate, and in the THz box, that is a vacuum chamber.

### 5.1 $\text{CuGeO}_3$

The first measurements have been performed on a  $\text{CuGeO}_3$  crystal.  $\text{CuGeO}_3$  has an orthorhombic crystal structure and at room temperature the lattice parameters are  $a=4.81\text{\AA}$ ,  $b=8.47\text{\AA}$ ,  $c=2.94\text{\AA}$  and space group  $\text{Pbmm}$  ( $x \parallel a, y \parallel b, z \parallel c$ ) [17] [18].

The building blocks of the crystal structure are edge-sharing  $\text{CuO}_6$  octahedra and corner-sharing  $\text{GeO}_4$  tetrahedra stacked along the  $c$ -axis of the crystal and resulting in  $\text{Cu}_2^+$  and  $\text{Ge}_4^+$  chains parallel to the  $c$ -axis [19]. These chains are linked together via the  $O$  atoms and form layers parallel to the  $b$ - $c$  plane weakly coupled along the  $a$ -axis. This structure is shown in Figure 5.1.

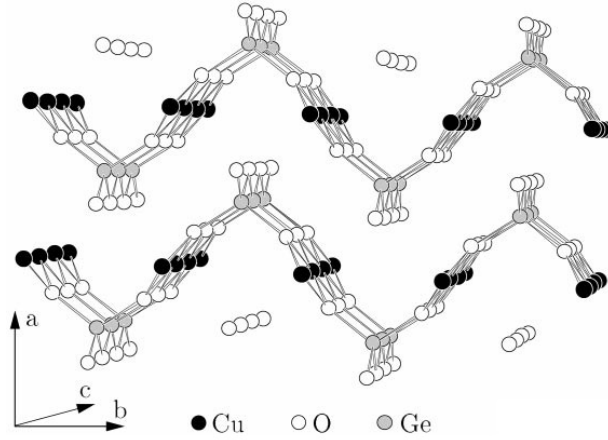


**Figure 5.1:** *Crystal structure of CuGeO<sub>3</sub>.*

Infrared reflectivity measurements of pure CuGeO<sub>3</sub> [19] with the THz electric field parallel to the crystal b-axis and c-axis, show signatures of the infra-red active phonon modes. We report the two spectra in Figure 5.2. Three phonons are detected when light is polarized along the c-axis (167, 528 and 715 cm<sup>-1</sup> which correspond to 5, 15.8 and 21.5 THz), and five along the b-axis (48, 210, 286, 376 and 766 cm<sup>-1</sup> or 1.45, 6.3, 8.6, 11.3 and 23 THz).

The frequency range of the THz pulses produced in our setup is between about 0 and 3 THz that correspond to 0 and 100 cm<sup>-1</sup>. We can see from Figure 5.2 that in this range we can observe only one phonon at about 1.5 THz only when the THz electric field is parallel to the b-axis.

With *CuGeO<sub>3</sub>* sample we have performed two measurements, both at THz beam normal incidence. The first with the THz electric field parallel to the crystal b-axis and the second with THz field parallel to the c-axis.

In Figure 5.3 and 5.4 we show the measurements performed with the THz polarization parallel to the crystal b-axis and c-axis. In the first case, with  $E_{THz} \parallel$  b-axis, we can see the absorption peak at 1.5 THz which correspond to the first phonon mode of Figure 5.2. Then, if we set the THz polarization along the c-axis we can see a small absorption at 2.8 THz. This absorption can be read as the left end part of the phonon at 5 THz.

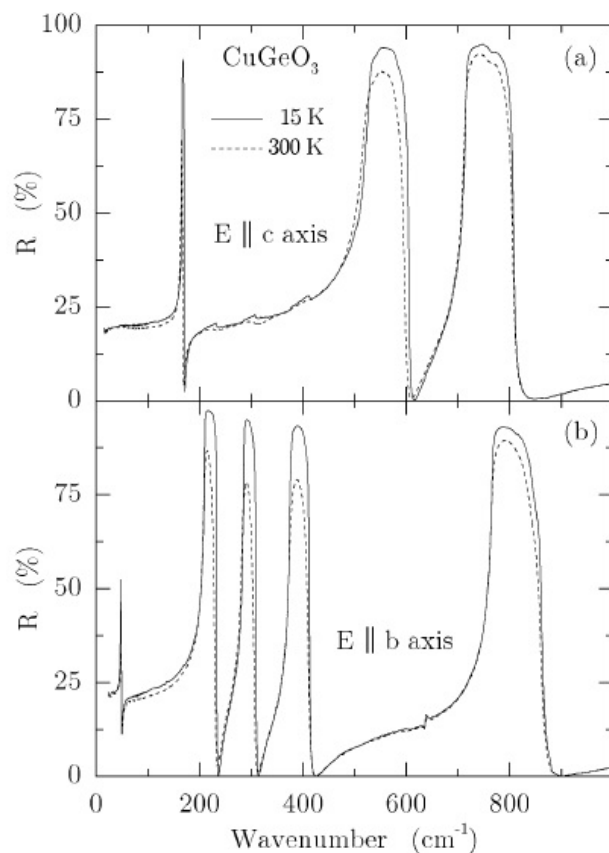


**Figure 5.2:** Reflectivity of a single crystal of pure  $\text{CuGeO}_3$  as a function of wave number at two different temperatures (300 and 15 K). The spectra are shown for light polarized along the  $c$ -axis (a), and the  $b$ -axis (b) of the crystal.

## 5.2 Organic-Inorganic Hybrid

We now observe the THz absorption of  $(\text{C}_6\text{H}_5\text{CH}_2\text{CH}_2\text{NH}_3)_2\text{CuCl}_4(\text{PEACuCl})$ , an organic-inorganic hybrid material that is the crystalline combination of typical inorganic structures with organic molecules [20]. This material has a large inorganic connectivity, in which the inorganic part has a structure reminiscent of the perovskites [21]. The well connected inorganic constituents provide robust interactions leading to functional electronic, magnetic, and optical properties. This family of organic-inorganic hybrids has in particular been widely studied for their intriguing magnetic properties [22] and the structural phase transitions

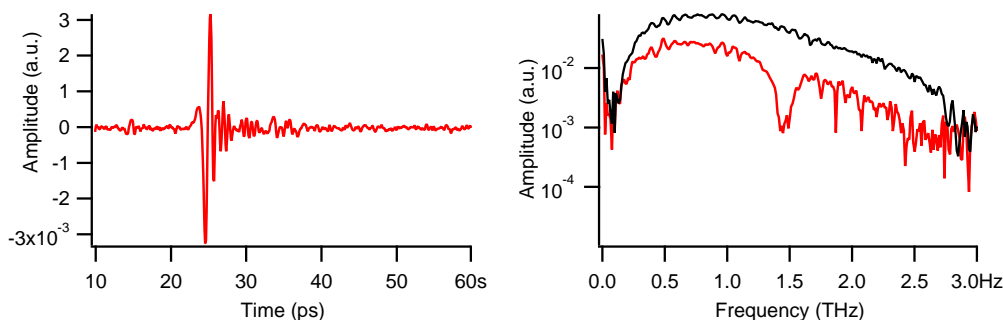


**Figure 5.3:** THz measurement with  $\text{CuGeO}_3$  sample with electric field parallel to the  $b$ -axis (red line). The black line is the reference spectrum with no sample.

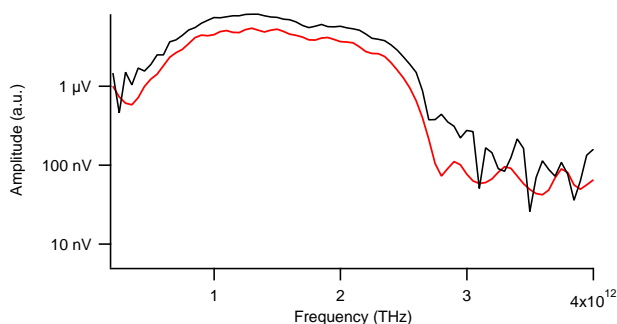


**Figure 5.4:** THz measurement with  $\text{CuGeO}_3$  sample with electric field parallel to the  $c$ -axis.

[23][24].

The layered hybrids have a simple structure [21]: the corner sharing inorganic octahedra form isolated chessboard-like layers; the organic molecules fill the cavity left between the octahedra, attached on both sides of the layer ammonia head. Typically at room temperature two types of orthorhombic structures are observed [25]: a more symmetric one ( $\text{Cmca}$ ,  $D_{2h}^{18}$ ), like for manganese compounds and a more distorted one ( $\text{Pbca}$ ,  $D_{2h}^{15}$ ), typical of copper.

We now present two measurements on this hybrid sample in normal incidence with two different sample orientation which differ by 90 degrees. The two pulses in time and frequency domain are shown in Figure 5.5. Comparing the two spectra (red and blue lines) with the reference spectrum (black line) we observe a common large absorption band from 1.5 THz and one smaller absorption band at about 0.5 THz. This last absorption is more

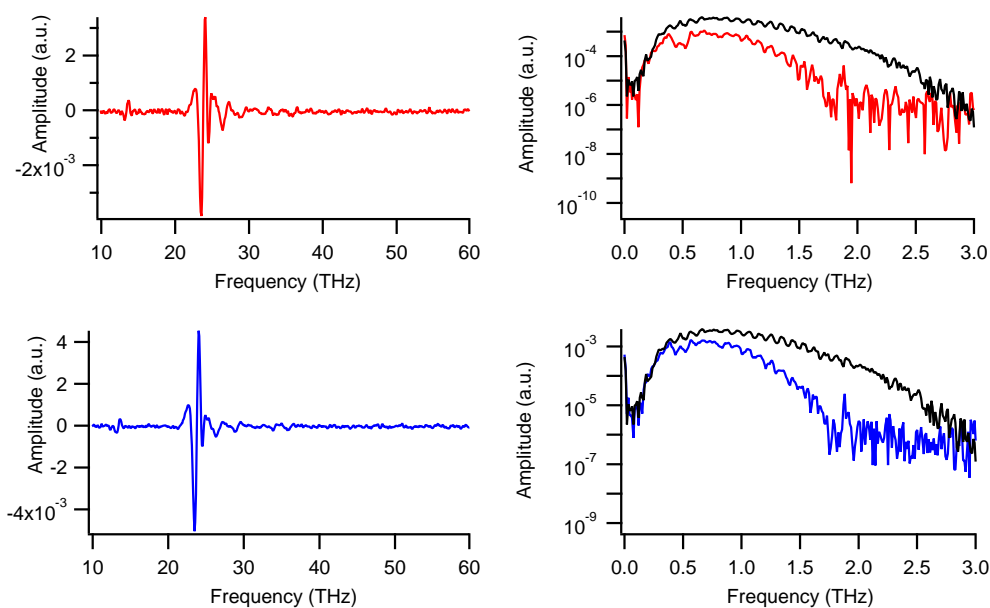


**Figure 5.5:** THz measurement with hybrid sample in time and frequency domain at two different sample orientations. The black line is the reference spectrum.

visible in the first measurement (red line) indicating the presence of a phonon mode along one particular direction of the crystal axes.

In order to better compare the two different absorption spectra we consider the ratios with the reference spectrum shown in Figure 5.6a. It is clear that the first measurement (red line) has a larger absorption and that the spectrum structure is similar in the two cases.

Figure 5.6b shows the ratio between the two transmissions to highlight the differences of the structures.

## 5.3 Biological Samples

The last measurements we now present have been performed on biological samples, the sucrose ( $C_{12}H_{22}O_{11}$ ) and a sample of human blood. The first measurement is with a sucrose tablet sample 1cm thick. We show the results in Figure 5.7. We can see the evident large band absorption from 1 to 2.5 THz with many tight-band absorption peaks, the main are at 1.2, 2.1, 2.4 and 2.6 THz.

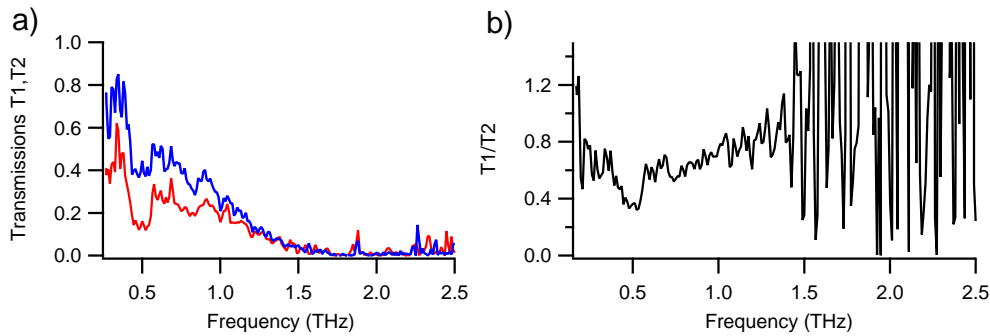


**Figure 5.6:** a) Transmission of the two sample orientations b) Ratio of the two transmissions.

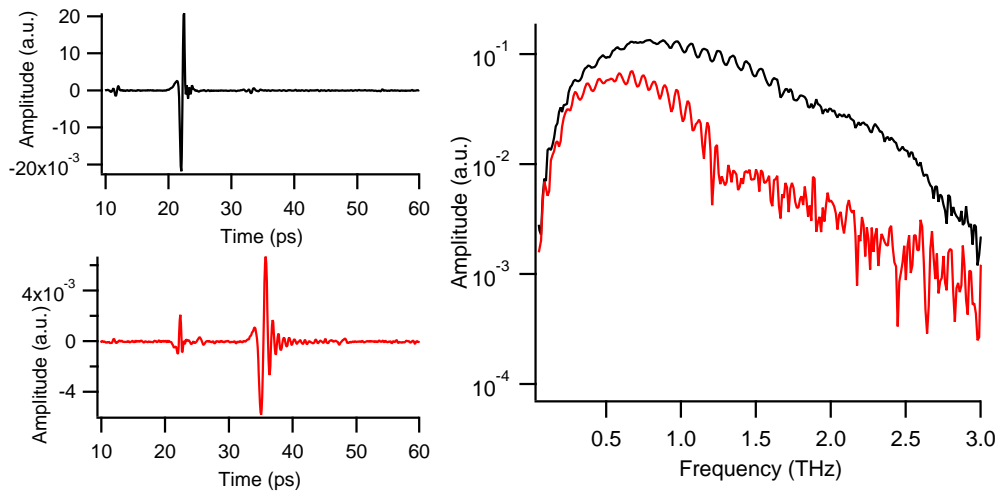


**Figure 5.7:** Reference (black line) pulse and sucrose measurement (red line).

The THz measurement of human blood on human blood has been performed on a dry blood drop placed on a paper sheet, then the reference is with only one paper sheet sample. In Figure 5.8 are shown the two spectra. We don't see any absorption peak but a non constant absorption all over our frequency range. The ratio between these spectra that is the transmission in frequency domain is shown in Figure 5.8b, in this way we can see the transmission trend in function of frequency. The transmission decreasing can be compared to the absorption coefficient of the various blood components of Figure 5.8c [26]. Unfortunately we can't calculate the absorption coefficient

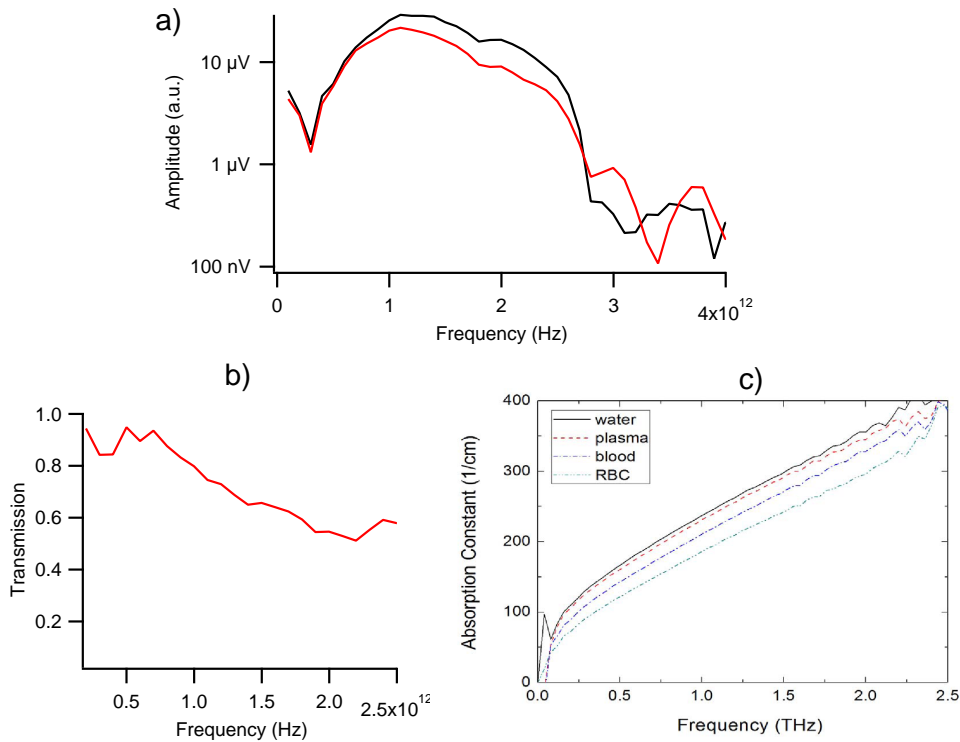


**Figure 5.8:** a) Reference spectrum (black line) and blood spectrum (red line) b) Transmission spectrum c) Absorption constants of water, whole blood, plasma, and red blood cells [26].

of our blood sample because we don't know the sample thickness because the dry blood drop on paper sheet has no uniform thickness and we don't know the behaviour at the blood-paper interface. However it is also useful the comparison between transmission and absorption coefficients. Figure 5.8c shows the absorption coefficients of whole blood, plasma, and red blood cells which have a common trend. These trend qualitatively matches very well with the transmission of our sample shown in Figure 5.8b.

# Conclusions

The aim of this work has been the realization of a setup for time resolved terahertz spectroscopy at room temperature. For the generation and the detection of the THz pulses we employed optical techniques. We explained in details the optical rectification process. This effect at the basis of the production of THz pulses using ultrashort laser pulses. Then we presented the detection process which exploit the electro-optic effect of a second ZnTe crystal. This process allows the direct measurement of the THz electric field which implies a considerable advantage as compared to conventional spectroscopy, since information about the amplitude and the phase of the electric field can be simultaneously retrieved. We showed that, using THz time domain spectroscopy, both the real and imaginary parts of the response functions of the sample are obtained directly from its amplitude and phase informations and without the need of Kramers-Kronig transforms.

We performed measurements with different material. The first sample is  $\text{CuGeO}_3$  which shows different behaviour depending on the polarization of THz beam. We observed the absorption related to a phonon mode at 1.5 THz when the polarization of THz field was parallel to the b-axis of the crystal. The second sample was an hybrid organic-inorganic material and also in this case we performed two measurements with different and orthogonal THz polarizations. We observed two different kinds of absorption: a common large absorption band from 1.5 THz and a smaller one at about 0.5 THz that is different in the two different polarizations, indicating the presence of a phonon mode along one particular direction of the crystal axes. The last measurements we performed are with biological samples: sucrose and human blood. Sucrose showed evident large band absorption from 1 to 2.5 THz with many small absorption peaks. With the human blood sample we saw an absorption increasing over the whole frequency range.

This setup is only the first step of a more complex work. In fact, the present scheme for THz generation and detection can be straightforwardly upgraded to perform non-equilibrium time resolved terahertz spectroscopy measurements. This is possible adding a third beam line which is the pump line in order to perform optical pump - terahertz probe measurements.

An additional improvement of this setup will be also the introduction of the cryostat, a device that allows to maintain the sample at cryogenic temperatures.

With these two improvements it will be possible to perform pump-probe THz measurements at low temperature. This technique allows the study of systems exhibiting phase transitions at low temperatures in which a meV gap in the density of states opens. It will be possible to measure the optical properties directly on the energy scale of the gap and with pump-probe spectroscopy we will be able to externally perturb the gap and directly measure its recovery dynamics.

This work opens intriguing perspectives in the field of materials driven out of equilibrium by ultrashort light pulses.

# Bibliography

- [1] D. H. Auston, Subpicosecond electro-optic shock waves, *Appl. Phys. Lett.* 43 (1983), 713-715.
- [2] D. H. Auston, K. P. Cheung, and P. R. Smith, Picosecond photoconducting Hertzian dipoles, *Appl. Phys. Lett.* 45 (1984), 284.
- [3] Yun-Shik Lee, *Principles of Terahertz Science and Technology*, Springer.
- [4] *Terahertz Spectroscopy principles and applications*, CRC press, 2008.
- [5] T.R. Globus, D.L. Woolard, T. Khromova, T.W. Crowe, M. Bykhovskaia, B.L. Gelmont, J. Hesler, A.C. Samuels, *THz-Spectroscopy of Biological Molecules*, *J. Phys. Chem.* (2003).
- [6] S W Smye et al 2001 *Phys. Med. Biol.* 46 R101.
- [7] A. Giles Davies et al, *Terahertz spectroscopy of explosives and drugs*, 2008.
- [8] P. Knobloch et al 2002 *Phys. Med. Biol.* 47 3875.
- [9] Martin Dressel, Natalia Drichko, Boris Gorshunov, and Andrei Pimenov, *THz Spectroscopy of Superconductors*, *IEE J.* 2008.
- [10] Robert W. Boyd, *Nonlinear Optics*, Second Edition, Academic Press.
- [11] G. Gallot, J. Zhang, R. W. McGowan, T.-I. Jeon, and D. Grischkowsky, *Appl. Phys. Lett.* 74, 3450 (1999).
- [12] E. Hecht, *Optics*, Fourth Edition, International Edition.
- [13] MIRA900 Modelocked Ti:Sapphire Lasers Data Sheet.

- 
- [14] Nicky Dean, *Electronic and Structural Dynamics of Complex Materials*, 2010.
- [15] Toshiaki Hattori, Hikaru Kumon and Hideaki Tamazumi, *Terahertz Spectroscopic Characterization of Paper*.
- [16] Payam Mousavi, Frank Haran, David Jez, Fadil Santosa and John Steven Dodge, *Simultaneous composition and thickness measurement of paper using terahertz time-domain spectroscopy*.
- [17] S. Pagliara, F. Parmigiani, P. Galinetto, A. Revcolevschi, and G. Samoggia, *Phys. Rev. B* 66, 024518 (2002).
- [18] H. Vollenkle, A. Wittmann, H. Nowotny, *Monatsh. Chem.* 98 (1967) 1352.
- [19] A. Damascelli, D. van der Marel, F. Parmigiani, G. Dhahlenne and A. Revcolevschi, *Infrared reflectivity of pure and doped CuGeO<sub>3</sub>*, *Physica B* 244 (1998) 114-120.
- [20] Antonio Caretta, Rany Miranti, Alexey O. Polyakov, Remco W. A. Havenith, Thomas T. M. Palstra, and Paul H. M. van Loosdrecht, *Low-frequency raman study of the ferroelectric phase transition in a layered CuCl<sub>4</sub>-based organic-inorganic hybrid*, submitted.
- [21] D. Mitzi, *J. Chem. Soc., Dalton Trans.* , 1 (2001).
- [22] L. J. de Jongh and A. R. Miedema, *Adv. Phys.* 23, 1 (1974).
- [23] K. S. Aleksandrov and J. Bartolome, *Phase Transit.* 74, 255 (2001).
- [24] D. B. Mitzi, *Prog. Inorg.Chem.* 48, 1 (1999).
- [25] J. Petzelt, *J. Phys. Chem. Solids* 36, 1005 (1975).
- [26] Kiyoungh Jeongab, Yong-Min Huhab, Sang-Hoon Kimb, Yeonji Parkb, Joo-Hiuk Sonc, Seung Jae Ohb, and Jin-Suck Suh, *Characterization of Blood Cells by Using Terahertz Waves*, *IEEE* (2011).